

# **Deformable Image Registration Based on Tool-constrained Organ Modeling**

March 2017

Nadhifa Ayunisa

# Deformable Image Registration Based on Tool-constrained Organ Modeling

Nadhifa Ayunisa

## Abstract

Image registration is one of image processing techniques which is fundamental to the process of analyzing and understanding medical images. In radiotherapy, deformable image registration (DIR) has been used to support and assess cumulative dose distribution included in treatment planning. In the case of cervical cancer treatment, organ deformation is greatly caused by involvement of insertion of radiotherapy tool inside target organ uterus, which leads to difficulties in obtaining anatomically proper registration result. Previous methods in DIR have been implemented to solve organ alignment in medical images, however, these methods do not deal with external physical intervention on organ like what occurs during tool insertion.

This study proposes integrated method to solve image alignment for cervical cancer radiation treatment case by combining intensity-based image registration and biomechanical simulation using finite element method (FEM). Radiotherapy tool inserted into target organ is used to estimate correspondence between input images. By using this correspondence as displacement constraint, finite element analysis is employed to calculate organ deformation. Intensity-based cost function is extended with a new term coming from organ deformation result to provide correction from biomechanical viewpoint in image registration, with the aim that a better alignment is produced especially in target organ area.

In this thesis, the combined registration method is constructed then experimented on X-ray CT images of both phantom and real woman pelvis undergoing radiation treatment. Registration accuracy shows an average error of  $7.717 \pm 2.5419$  mm in 3D Euclidean for phantom image and uterus similarity value of  $0.513 \pm 0.223$  for clinical image.

**Keywords :** Deformable image registration, X-ray CT, FEM, Biomechanical simulation, Radiotherapy tool, Cervical cancer, Uterus

# Contents

<b>Chapter 1</b>	<b>Introduction</b>	<b>1</b>
<b>Chapter 2</b>	<b>Deformable Image Registration Method for Radiation Therapy</b>	<b>4</b>
2.1	Radiation Therapy in Cervical Cancer . . . . .	4
2.2	Intensity and Hybrid Method in Deformable Image Registration . . . . .	5
2.3	Proposed Method in Current Study . . . . .	10
<b>Chapter 3</b>	<b>Biomechanically-combined Deformable Image Registration</b>	<b>11</b>
3.1	Summary of System . . . . .	11
3.2	Radiotherapy Tool as Corresponding Location . . . . .	13
3.3	Biomechanical Simulation with Finite Element Method . . . . .	17
3.4	Incorporating Biomechanical Term into Intensity Registration . . . . .	19
<b>Chapter 4</b>	<b>Image Registration and Biomechanical Simulation as an Integrated Process</b>	<b>25</b>
4.1	Material and Data . . . . .	25
4.2	Experiment . . . . .	30
4.3	Result and Evaluation . . . . .	32
<b>Chapter 5</b>	<b>Conclusion</b>	<b>57</b>
	<b>Acknowledgement</b>	<b>58</b>
	<b>Bibliography</b>	<b>59</b>
	<b>Achievement</b>	<b>64</b>

# List of Figures

1.1	General concept of system. . . . .	3
2.1	Radiation treatment method for cervical cancer. . . . .	5
2.2	Result of masked high-contrast regions . . . . .	6
2.3	Result of the FEM correction framework . . . . .	7
2.4	Adaptive mesh refinement strategy . . . . .	8
2.5	Result of organ deformation modeling . . . . .	9
3.1	Workflow of system. . . . .	12
3.2	Intensity mapping for the deformed structure. . . . .	13
3.3	Corresponding location between input images. . . . .	13
3.4	Flow of centerline extraction. . . . .	15
3.5	Flow of skeletonization algorithm used to extract centerline. . . . .	16
3.6	Fixed and moving image correlation. . . . .	19
3.7	Organ structure from moving image to deformed structure. . . . .	20
3.8	Free-form deformation based on B-splines. . . . .	23
3.9	Multi-resolution strategy. . . . .	24
4.1	Woman pelvic phantom used to obtain phantom images. . . . .	26
4.2	Axial view of phantom images. . . . .	26
4.3	Coronal view of phantom images. . . . .	26
4.4	Sagittal view of phantom images. . . . .	27
4.5	Axial view of clinical images. . . . .	28
4.6	Coronal view of clinical images. . . . .	28
4.7	Sagittal view of clinical images. . . . .	28
4.8	Segmented target organ in clinical images. . . . .	29

4.9	Three dimensional visualization of segmented target organ. . . . .	29
4.10	Corresponding point selection in preliminary experiment. . . . .	30
4.11	Uterus model before simulation. . . . .	31
4.12	DSC as a measurement of spatial overlap. . . . .	33
4.13	Hausdorff distance in image matching. . . . .	33
4.14	Displacement estimation from moving image to fixed image. . . . .	34
4.15	Deformed structure of phantom uterus. . . . .	35
4.16	Target structure of phantom uterus. . . . .	35
4.17	Comparison of phantom image before and after intensity registration. . . .	36
4.18	Comparison of phantom image before and after combined registration. . .	36
4.19	Marker $mp_0$ from sagittal view. . . . .	38
4.20	Marker $mp_1$ from sagittal view. . . . .	39
4.21	Marker $mp_2$ from sagittal view. . . . .	40
4.22	Pre-processed volume of uterus(left) and applicator(right) from P8 image pair . . . . .	41
4.23	Extracted centerline of uterus(left) and applicator(right) from P8 image pair	42
4.24	Result of extracted centerline from other patient images. . . . .	42
4.25	Comparison of deformed structure and input image structure from phan- tom data. Color bar represents displacement in millimeters . . . . .	43
4.26	Comparison of deformed structure and input image structure from one of patient data. Color bar represents displacement in millimeters . . . . .	44
4.27	Result of combined registration for phantom image . . . . .	45
4.28	Result of combined registration for one of patient image . . . . .	45
4.29	Six markers used for the registration evaluation. . . . .	47
4.30	Comparison of registration accuracy in all directions . . . . .	48
4.31	Comparison of registration accuracy in 3D Euclidean . . . . .	48
4.32	Hausdorff distance evaluation for each pelvic organ in clinical data . . . .	50
4.33	DSC evaluation for each pelvic organ in clinical data . . . . .	51
4.34	Comparison of deformed image and target structure with the good organ overlap. . . . .	53

4.35 Comparison of deformed image and target structure with the poor organ overlap. . . . .	54
4.36 Comparison of hausdorff distance from the combined and intensity method	55
4.37 Comparison of DSC from the combined and intensity method . . . . .	55

# List of Tables

4.1	Properties of phantom images. . . . .	27
4.2	Properties of clinical images. . . . .	28
4.3	Properties for simulation. . . . .	31
4.4	Registration configuration. . . . .	31
4.5	PC specification. . . . .	31
4.6	Location comparison for marker $mp_0$ . . . . .	38
4.7	Location comparison for marker $mp_1$ . . . . .	39
4.8	Location comparison for marker $mp_2$ . . . . .	40
4.9	Evaluation for registration on phantom image. . . . .	46
4.10	Evaluation for combined registration on patient image. . . . .	49

# Chapter 1 Introduction

Medical imaging technology, including its correlating image processing technique, has made a remarkable impact on healthcare field. Image registration is one of image processing techniques whose primary goal is to find corresponding anatomical or functional locations between two or more images [1]. Establishing the correspondence of spatial information in medical images and equivalent structures in the body is fundamental to the process of analyzing and understanding medical image and its underlying information [2]. Therefore, image registration has become an important process for a large number of applications. In performing image registration, several types of transformation can be applied. Rigid registration, in which image is globally transformed, only changes position and orientation of the image. In 3D (three dimensional) to 3D registration, rigid registration gives six degrees of freedom. However, for more complex local anatomical differences between two medical images, registration process with more degree of freedom is needed. Deformable (non-rigid) image registration, in which image is more locally transformed, can handle changes in shape or size of objects in images.

Along with its development, various algorithms and frameworks in deformable image registration have been investigated to find the most optimum method for many clinical cases. Image information, such as features (points, lines, curves, edges, shape of objects, etc.) and image intensity can be used as the important element for registration [3]. However, depending on how large the deformation between two or more images and how different image information is, methods based on image information only can be computationally expensive and inefficient [4].

In radiation treatment planning, deformable image registration (DIR) is widely employed especially in the process of generating cumulative dose distribution. Effective radiation treatment in the case of cervical cancer typically consists of two types of treatment,

one is a treatment that applies radiation dose from outside patient's body, and the other one is called brachytherapy, which is a treatment that applies higher dose of radiation inside patient's body by using a certain treatment tool. The insertion of tool in brachytherapy treatment introduces uncertainties in anatomical variations mainly because of the large deformation in organs. This factor, along with the existence of two different treatment methods, are the main factors that cause the process of correlating pelvic images in cervical cancer treatment challenging [5,6]. The inexistence of some voxels intensity in treatment without tool insertion also leads to the challenge in finding correspondence between both treatment images, hence the difficulties in obtaining anatomically proper registration result by only intensity information.

Attempts in correlating physical characteristics into image registration have been done in many ways, one of which is done by making use of organ shape information similar to what implemented in ANACONDA algorithm [7]. The other way is done by deformation simulation using finite element method (FEM). This method produces highly accurate solutions to non-linear equations under realistic conditions when given sufficient resolution of the geometry of interest [2]. Finite element method has been commonly used as a foundation for evaluating deformable image registration, such as in surface-constrained non-rigid registration for dose monitoring in prostate cancer radiotherapy [8] and in FEM-based evaluation of deformable image registration for radiation therapy [9]. It is also used to model target organs in combined deformable image registration method for some certain applications, such as lung deformation case [10–12], prostate cancer [13] and liver [14]. However, these previous frameworks do not deal with large deformation from external physical intervention, as what occurs in brachytherapy during cervical cancer treatment. For cervical cancer case itself, registration methods that are applied in previous researches such as [15] and [16], are mainly still done with intensity-based method. There are also methods that use shape information of organ for cervical cancer case such as [6] and [17], but the methods still need manual adjustment which means expertise in medical anatomy is needed to perform the registration.

For that reason, this study proposes an integrated method between intensity-based image registration and biomechanical simulation using finite element analysis by making use of

radiotherapy tool as a new approach to obtain spatial correspondence between images. The aim of this process is to solve image alignment, especially between images taken during different type of treatment (with and without tool) in cervical cancer case.

Figure 1.1 shows a general concept of this method. Image A and B represent two pelvic images from the same imaging modality in which Image A will be modified to be spatially aligned with Image B. Image A is taken during radiation treatment method without tool insertion, while Image B is taken during radiation treatment method involving insertion of tool inside of organ at risk. By making use of characteristic in the handled case as boundary conditions, biomechanical simulation is done to obtain deformed structure of target organ. The information from deformed target organ will be used as an additional parameter in the intensity-based combined registration. The combined registration is expected to result in a more aligned images compared to the intensity only registration, especially in the target organ area.

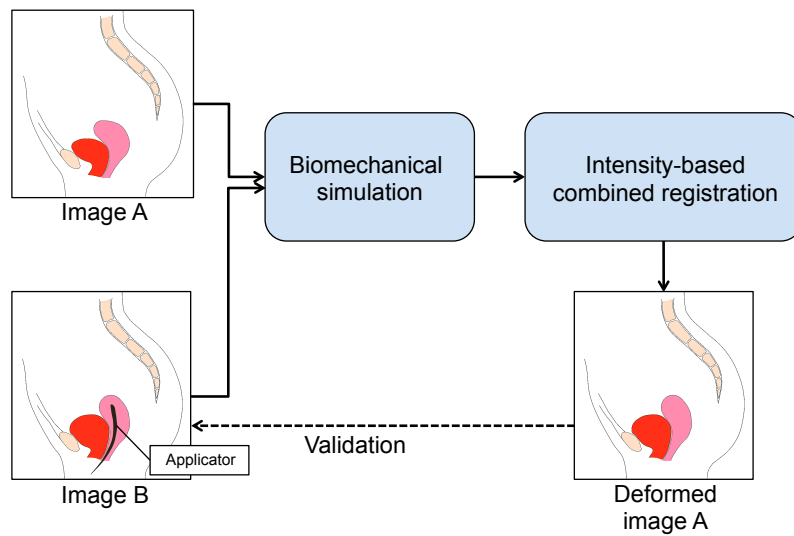


Figure 1.1: General concept of system.

In this thesis, the combined method between intensity and biomechanical simulation is presented and extended in order to be able to handle a wider variety conditions that likely happen in real patient image. Further, the developed method is experimented on both phantom and clinical data. Qualitative and quantitative evaluation based on overall image and specific information taken from target organ are also done to see the performance of the proposed combined registration, especially in comparison to the intensity only registration.

# **Chapter 2 Deformable Image Registration Method for Radiation Therapy**

## **2.1 Radiation Therapy in Cervical Cancer**

Deformable image registration is the problem of finding a displacement that makes one image spatially aligned to another image with a transformation model that has high flexibility capable of handling local deformation in image region. In radiotherapy, medical images with their respective dose are taken multiple times from the patient. In order to plan the treatment, cumulative radiation dose distribution is commonly calculated from these images. However, as there are many differences between these images including different patient positions and internal anatomical conditions, deformable image registration is needed to ensure the correctness of this calculation. [18]

In cervical cancer treatment [19] specifically, combination of two radiotherapy types is commonly used, namely external beam radiotherapy (EBRT), in which radiation dose is applied from outside patient's body, and intracavitary brachytherapy (ICBT), in which radiation dose is applied within targeted location inside patient's body by using a specific tool, called a brachytherapy applicator. Figure 2.1 illustrates the aforementioned two treatment methods.

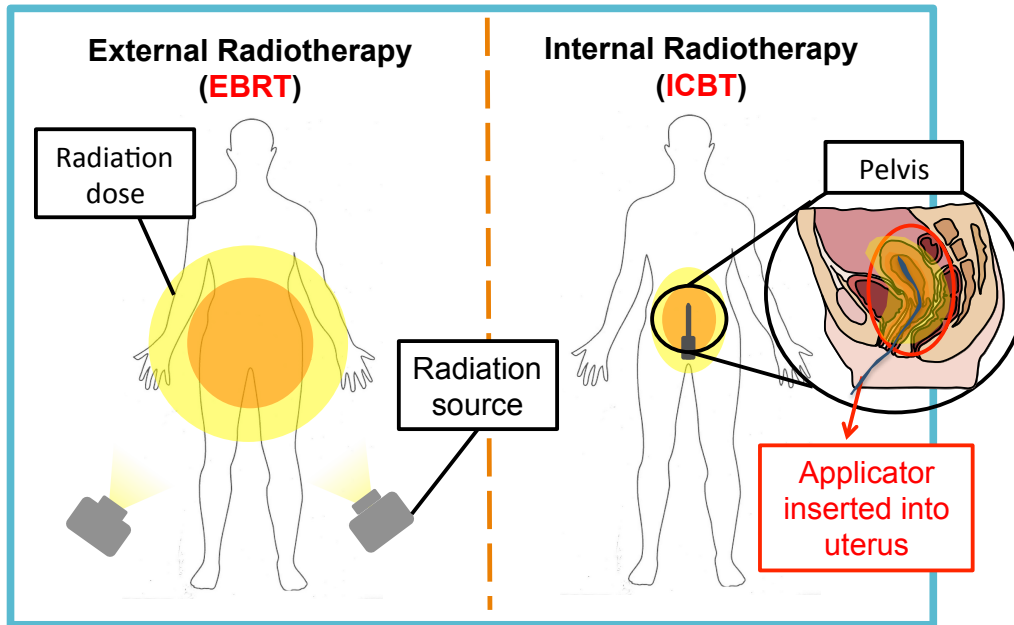


Figure 2.1: Radiation treatment method for cervical cancer.

To perform deformable image registration, image-based registration method by using image voxel intensity is commonly employed. Another method is to directly deform the image by using FEM elastic analysis. There are many uncertainties related to brachytherapy for cervical cancer due to several factors including anatomical variations and applicator [5]. Therefore, there are difficulties in obtaining a good deformable image registration result especially if only intensity information is used. FEM has been used in correlation with intensity-based deformable image registration in order to obtain better aligned images.

## 2.2 Intensity and Hybrid Method in Deformable Image Registration

FEM as one of the attempt to improve deformable image registration method can be used in various ways and for various cases. The following subsections introduce several previously studied deformable image registration with FEM as one of the processes, along with the aim of the methods itself.

### 2.2.1 FEM for DIR Error Correction

In FEM-corrected deformable image registration framework [20], FEM is used to improve the accuracy of an intensity-based image registration algorithm in low-contrast regions. Image registration based on demons algorithm [21], which is a widely applied registration method based on optical flow is performed in this framework.

At first, high-contrast regions in which intensity-based image registration might perform better performance are identified. Depending on what image the framework is used, criteria to identify these regions is determined by a certain threshold value, in which this value depends on the standard deviation of the image intensity in target image. Figure 2.2 shows results of this process on lung and prostate cases.



(a) Lung CT image



(b) Prostate CT image

Figure 2.2: Result of masked high-contrast regions [20].

Deformation vector field (DVF) represents the deformation in input image after transformation is applied to it. Tetrahedral mesh will then be refined recursively in the previously explained masked regions to obtain sufficient number of driving nodes. This information, along with the deformation vector field obtained from intensity-based registration with demons algorithm, will be used as a base for finite element modeling. From the process, DVF from FEM is obtained. Figure 2.3 shows the result of correction framework in prostate case and its comparison with the result of intensity-based image registration only.



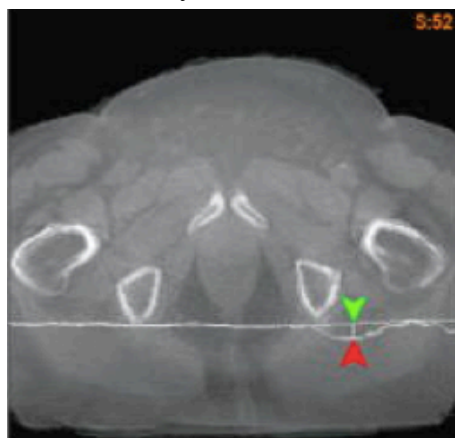
(a) Lung CT image



(b) Transformed target image using intensity-based method



(c) Transformed target image using FEM



(d) Positional difference between (b) and (c)

Figure 2.3: Result of the FEM correction framework [20].

This study shows that FEM can be integrated with intensity-based image registration algorithms to improve registration accuracy, however, FEM in this study is intended to solve low-contrast problem in image rather than geometrical problem of target organ.

## 2.2.2 Adaptive FEM Method for Image-based DIR

In elastic model for medical image registration used in framework [4], adaptive strategy in mesh refinement for elastic registration model using FEM is performed. This framework uses FEM elastic model that computes a deformation field to satisfy both elasticity constraint and similarity metric constraint, in which in this method, similarity gradient is used to obtain external force field to calculate elastic deformation. There are two major processes in the framework, namely adaptive mesh refinement and deformation field computation. Region intensity variance and region deformation in the image are determined to decide whether the mesh in sub-region should be refined. The larger intensity variances in an image region, the finer resolution of mesh is generated. Figure 2.4 shows adaptive mesh refinement strategy in the framework.

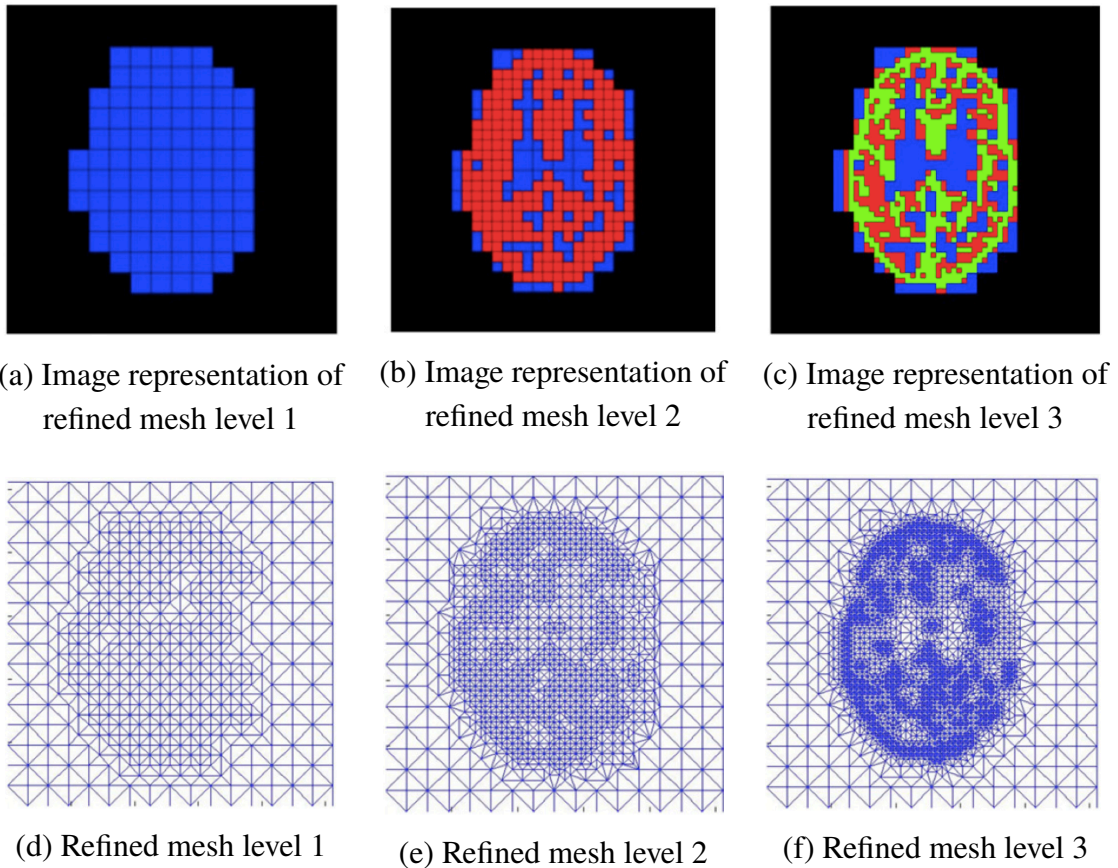
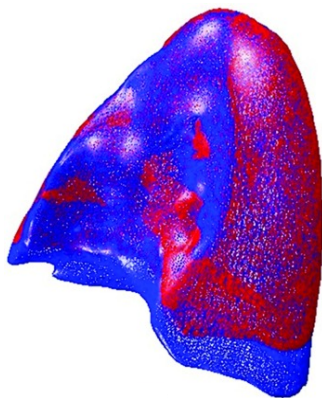


Figure 2.4: Adaptive mesh refinement strategy [4].

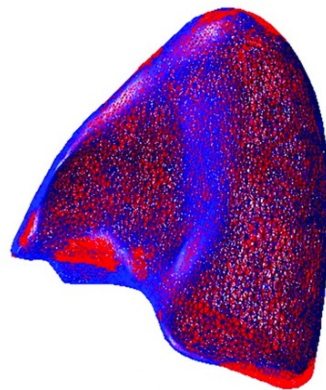
After the mesh is refined, global stiffness and external force matrices are calculated and nodal displacements are updated. For every converged metric value, the process will be repeated until the finest resolution of mesh is obtained. This study improves image registration by adaptively refine mesh for FEM, however, the FEM in this method is used to categorize image according to its regional intensity variance, and it is not used to model the targeted organ geometrically.

### 2.2.3 FEM for Modeling Organ Deformation

In lung deformation modeling framework [10], a combined method between varying intensity flow block-matching algorithm and finite element method for deformable image registration is performed. This framework is implemented for modeling in lung deformation to register end-expiratory (EE) phase to end-inspiratory (EI) phase of lung. In this method, intensity-based image registration of EE phase image to EI phase is used to estimate surface motion of lung, which then is used to estimate its elasticity distribution via a quasi-Newton optimization approach. Figure 2.5(a) shows the differences between EI surface mesh and EE surface mesh before registration process. EE surface is then deformed to match EI surface, in which the comparison between the deformed EE surface and EI surface is shown in Figure 2.5(b). In both figures, EI surface mesh is drawn in blue and EE surface is drawn in red.



(a) Lung overlap before registration



(b) Lung overlap after registration

Figure 2.5: Result of organ deformation modeling [10].

This study integrates organ modeling and intensity registration, as well as considering inhomogeneity of organ's tissue, however the study is intended for lung motion and it uses surface motion as boundary condition without considering any external intervention into organ.

### **2.3 Proposed Method in Current Study**

In previous studies, physical characteristics in form of finite element method are used to improve accuracy of image-based registration, especially when it comes to problem with low-contrast region, or to model organ deformation from physiological phenomena without external disturbance. However, these methods do not provide a solution for organ deformation that is caused by artificial intervention. In this study, integrated approach between image information-based DIR and physical model is proposed. Image information that is chosen as fundamental element for DIR in this framework is image intensity. Physical model based on finite element method is employed to obtain deformed structure of organ, which then will be included in the cost function of combined registration as additional biomechanical term. The framework will be implemented to handle large deformation in organ from physical intervention, specifically for pelvic images during brachytherapy which includes applicator insertion in cervical cancer treatment. For some cases in target organ and its surrounding organs, namely uterus, bladder and rectum, the usage of intensity information to solve this large deformation does not give proper result. The proposed framework takes the physical intervention in target organ itself as advantageous information that represents organ deformation. Biomechanical term incorporated in the framework is expected to give correction and improve quality of organ alignment in images.

# Chapter 3 Biomechanically-combined Deformable Image Registration

## 3.1 Summary of System

Physical intervention in medical treatment can cause large and irregular deformation in organ. For such a case, image-based registration only is not suitable to handle anatomical changes between two or more clinical images. Further, three dimensional biomechanical simulation is needed to represent organ deformation volumetrically. Figure 3.1 shows the framework proposed in this study. In the proposed combination method, biomechanical simulation of organ is used to describe uterus motion during radiation therapy process. At first, two clinical images from the same imaging modality are used as input. EBRT image is used as moving image (or source image) and ICBT image, in which uterus is largely deformed by insertion of applicator, is used as fixed image (or target image). Moving image will be modified, while fixed image is used as a reference.

As a target organ, contour of uterus in EBRT image is extracted and discretized into tetrahedral elements during volumetric meshing. Dirichlet condition or given displacement is employed as boundary condition for finite element analysis, and it is determined by making use of brachytherapy characteristic, which is the insertion of tool inside uterus.

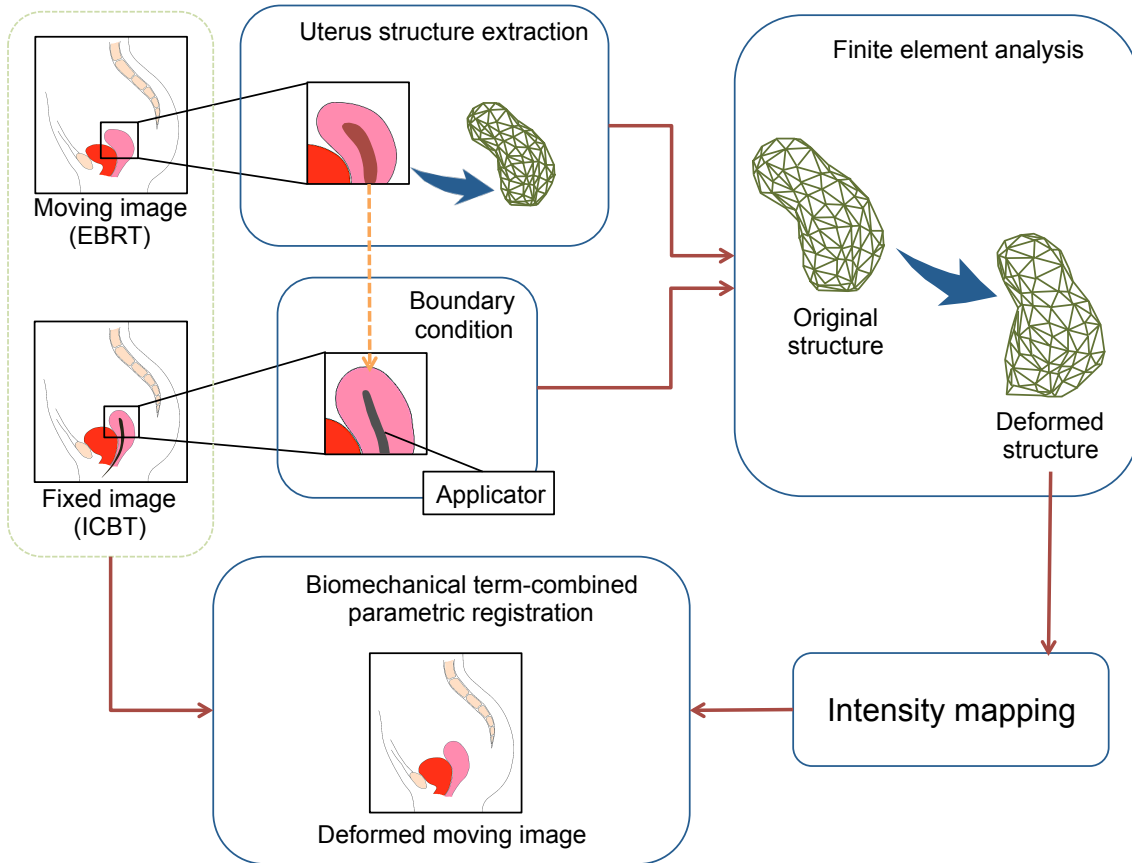


Figure 3.1: Workflow of system.

It is assumed that tool inserted into the uterus is in contact with the internal wall of uterus for the most part, therefore position of tool inside uterus in ICBT image and internal wall of uterus in EBRT image can be said corresponds to each other. This information is then used as displacement constraint to obtain a deformed uterus structure using finite element analysis. This will be described further in the subsequent section.

Each node in the obtained deformed uterus structure is mapped to obtain new intensity distribution as shown in Figure 3.2, and this information is combined to the previous intensity-only registration to provide correction from biomechanical point of view. This combined registration results in a deformed moving image which is spatially aligned with the fixed image, especially in target organ region.

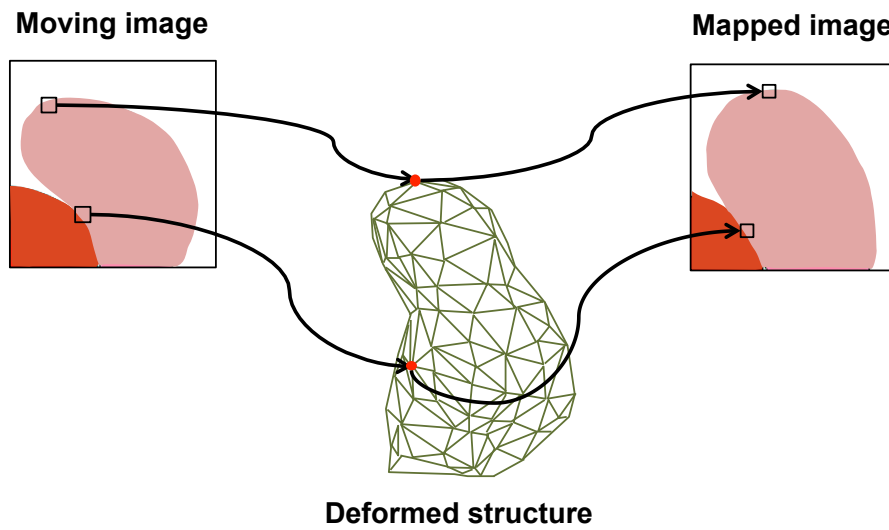


Figure 3.2: Intensity mapping for the deformed structure.

### 3.2 Radiotherapy Tool as Corresponding Location

In the combined method, information from the internal part of target organ is taken into advantage. By taking assumption that the shape of internal space of uterus, and hence, the overall uterus itself, changes exactly according to applicator, these locations are considered as corresponding location. Simplifying this location into series of points along the center of applicator volume in fixed image and center of uterus space in moving image, displacement between these points is then given as boundary condition for biomechanical simulation.

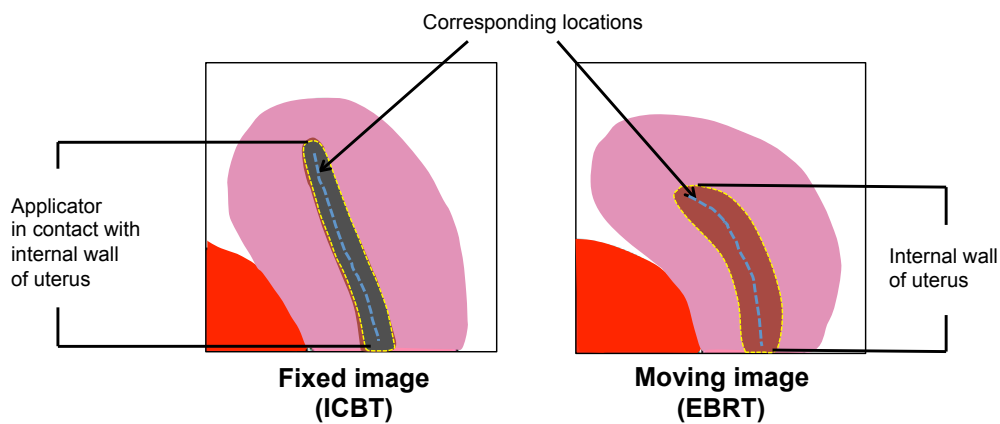


Figure 3.3: Corresponding location between input images.

Figure 3.3 illustrates the selection of corresponding location between fixed and moving images. In this figure, the blue lines in the fixed image represents center of applicator volume and that of the moving image represents center of uterus space. Figure 3.4 illustrates the process of taking centerline of selected corresponding location from the fixed image. Region of interest is decided such that all voxels in applicator area is included. In preliminary implementation, image segmentation based on three dimensional Canny edge detection [22] followed by image dilation and erosion is then performed to obtain binary image with only volume from which centerline would like to be extracted. In Canny edge detection, an edge point is defined in Equation (3.1)

$$\frac{\partial^2}{\partial \mathbf{n}^2} G * I = 0 \quad (3.1)$$

in which  $I$  is the intensity within an image,  $\mathbf{n}$  is a normal vector,  $G$  is Gaussian function and  $*$  is the convolution operator. The normal vector  $\mathbf{n}$  can be estimated from the smoothed gradient direction as shown in Equation (3.2) and 3D (three dimensional) Gaussian is defined in Equation (3.3).

$$\mathbf{n} = \frac{\nabla(G * I)}{|\nabla(G * I)|} \quad (3.2)$$

$$G(x, y, z; \sigma) = \frac{1}{(2\pi)^{3/2}\sigma^3} \exp\left(-\frac{x^2 + y^2 + z^2}{2\sigma^2}\right) \quad (3.3)$$

in which  $\sigma$  is the standard deviation. This binary image from segmentation result is used to calculate function of the distance field from which skeletonization based on fast marching methods [23] is applied.

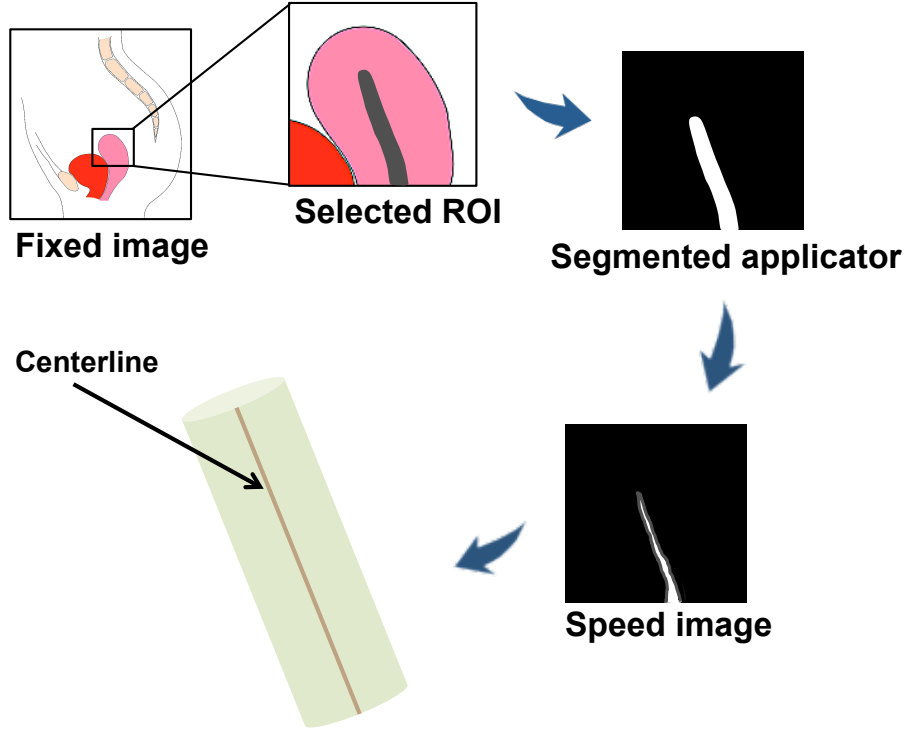


Figure 3.4: Flow of centerline extraction.

Centerline extraction uses a minimum-cost path problem defined in Equation (3.4) to find a path  $J$  at time  $t$  that minimizes cumulative cost  $W$ .

$$Q(\mathbf{x}) = \min_{J_{sx}} \int_0^L W(J(t)) dt \quad (3.4)$$

In this equation,  $J_{sx}$  is the set of all path from start point  $s$  to current position  $\mathbf{x}$ , and  $L$  is the distance between end point to start point along path  $J$ . Cost function  $W(\mathbf{x})$  here is the speed image as a function of the distance field, given by Equation (3.5)

$$W(\mathbf{x}) = \left( \frac{d(\mathbf{x})}{D} \right)^2 \quad (3.5)$$

in which  $d(\mathbf{x})$  is the distance value at position  $\mathbf{x}$  and  $D$  is maximum value in the distance field dataset.

Figure 3.5 shows summary of main steps in skeletonization algorithm [23,24] employed to obtain the centerline of applicator and internal wall of uterus. At first, point with the largest distance from object's volumetric boundary, the maximum value in distance field, as well as speed image is calculated by using Euclidean distance field. The speed image, which is a function of the distance field is used as input for fast marching method. This method is to calculate distance inside the object volume from the the point which has maximum value in distance field. The maximum value of this calculation result, or in other words, the obtained furthest point is used as start point of the branch. From here, back-tracking method is used to determine the other points of the branch. The series of points in the branch is the obtained skeleton or centerline of object which volume is input to the algorithm.

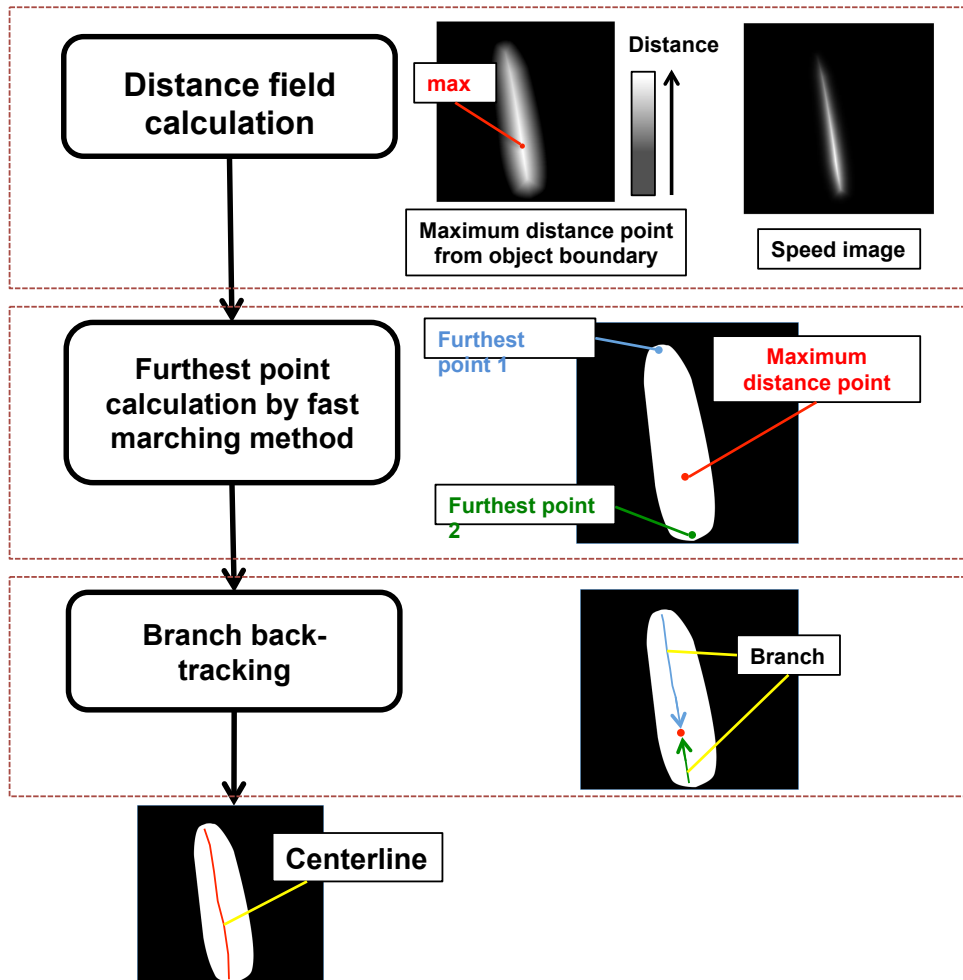


Figure 3.5: Flow of skeletonization algorithm used to extract centerline.

### 3.3 Biomechanical Simulation with Finite Element Method

Simulation for elastic object is performed to obtain a deformed target organ structure, which later will be incorporated into intensity registration to provide correction from biomechanical point of view. This simulation is done based on finite element method [25] with tetrahedral elements.

The displacement vector for a node in tetrahedral element is defined by three components,  $u_x$ ,  $u_y$  and  $u_z$ , as shown in Equation (3.6).

$$\mathbf{u} = \begin{bmatrix} u_x \\ u_y \\ u_z \end{bmatrix} \quad (3.6)$$

In the biomechanical simulation, deformation is obtained from the relationship between vector of forces acting on the node  $\mathbf{F}$ , stiffness matrix  $\mathbf{K}$  and nodal displacement  $\mathbf{u}$  as shown in Equation (3.7).

$$\mathbf{F} = \mathbf{K}\mathbf{u} \quad (3.7)$$

To simplify simulation process, organ is assumed to have linear elasticity, hence stiffness matrix  $\mathbf{K}$  in Equation (3.7) is a function with respect to material properties, Young's modulus and Poisson's ratio. This matrix can be obtained by Equation (3.8).

$$\mathbf{K} = \int_{\Omega} \mathbf{B}^T \mathbf{D} \mathbf{B} d\Omega \quad (3.8)$$

in which  $\Omega$  is the domain of the volumetric model,  $\mathbf{B}$  is matrix correlating to strain vector  $\boldsymbol{\varepsilon}$  and displacement  $\mathbf{u}$  with  $\mathbf{B}^T$  is its transpose, and  $\mathbf{D}$  is elasticity matrix.  $\mathbf{B}$  and  $\mathbf{D}$  are obtained by Equation (3.9) and (3.10).

$$\boldsymbol{\varepsilon} = \mathbf{B}\mathbf{u} \quad (3.9)$$

$$\mathbf{D} = \frac{E}{(1+\nu)(1-2\nu)} \begin{bmatrix} 1-\nu & \nu & \nu & 0 & 0 & 0 \\ \nu & 1-\nu & \nu & 0 & 0 & 0 \\ \nu & \nu & 1-\nu & 0 & 0 & 0 \\ 0 & 0 & 0 & \frac{1}{2}-\nu & 0 & 0 \\ 0 & 0 & 0 & 0 & \frac{1}{2}-\nu & 0 \\ 0 & 0 & 0 & 0 & 0 & \frac{1}{2}-\nu \end{bmatrix} \quad (3.10)$$

in which  $E$  is Young's modulus and  $\nu$  is Poisson's ratio values for the target organ.

As described previously, centerline of applicator in the fixed image and centerline of uterus in the moving image are taken as corresponding location, which is used to obtain boundary condition for simulation. Supposed  $\mathbf{c}_f$  is a point in the applicator centerline and  $\mathbf{c}_m$  is a point in the internal uterus space centerline, input nodal displacement constraint  $\mathbf{u}_c$  and force acting on that node  $\mathbf{f}_c$  in the volume mesh are calculated by Equation (3.11) and (3.12).

$$\mathbf{u}_c = \mathbf{c}_f - \mathbf{c}_m \quad (3.11)$$

$$\mathbf{f}_c = \mathbf{L}_{cc}^{-1} \mathbf{u}_c \quad (3.12)$$

in which  $\mathbf{L} = \mathbf{K}^{-1}$ ,  $\mathbf{L}_{cc}$  is the corresponding sub-matrix  $\mathbf{L}$  with the displaced input node,  $\mathbf{L}_{cc}^{-1}$  is its invers and  $\mathbf{u}_c$  is the known displacement. Given this information, displacement for all other nodes  $\mathbf{u}_o$  in the domain of volumetric target organ model can be computed by Equation (3.13).

$$\mathbf{u}_o = \mathbf{L}_{oc} \mathbf{f}_c \quad (3.13)$$

### 3.4 Incorporating Biomechanical Term into Intensity Registration

Incorporating biomechanical term into intensity registration is done by performing biomechanical simulation with the method explained in the previous section to obtain a new set of nodes describing the deformed organ, and then mapping each node in this structure to obtain new intensity distribution which then will be included in an additional term of similarity measure as the cost function. Similarity measure that is extended in the combined method is sum of squared differences (SSD) metric. Figure 3.6 shows the correlation between fixed and moving images and Equation (3.14) shows the SSD metric describing similarity measure between them.

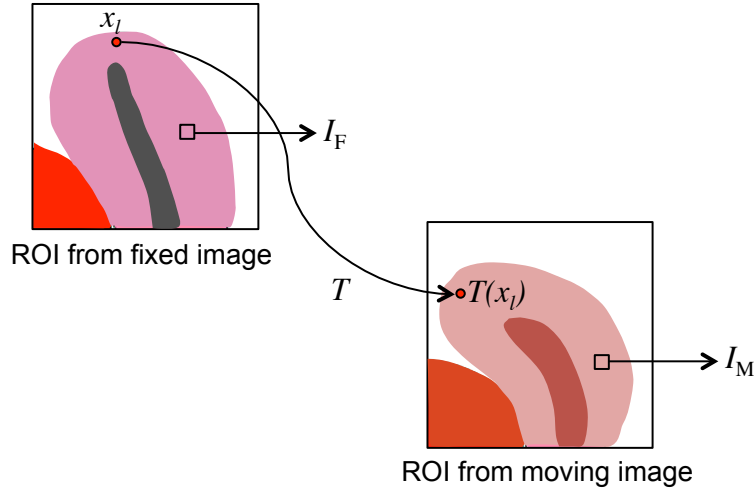


Figure 3.6: Fixed and moving image correlation.

$$SSD = \frac{1}{N} \sum_{l=1}^N (I_M(T(\mathbf{x}_l)) - I_F(\mathbf{x}_l))^2 \quad (3.14)$$

In both Figure 3.6 and Equation (3.14),  $\mathbf{x}_l$  represents image voxel position,  $T$  is transformation model used in registration,  $N$  is the number of image voxels,  $I_M(\mathbf{x}_l)$  is the intensity at voxel  $\mathbf{x}_l$  in moving image and  $I_F(\mathbf{x}_l)$  is the intensity at  $\mathbf{x}_l$  in fixed image.

Figure 3.7 shows the correlation between node position before and after biomechanical simulation with finite element analysis. The combined registration is basically solving

optimisation problem defined in Equation (3.15).

$$\hat{T} = \arg \min C(T; I_F, I_M) \quad (3.15)$$

In Equation (3.15),  $C$  is cost function to be minimized with regard to transformation  $T$ . Equation (3.16) is the extended cost function that describes similarity between images after result of biomechanical simulation is included in registration.

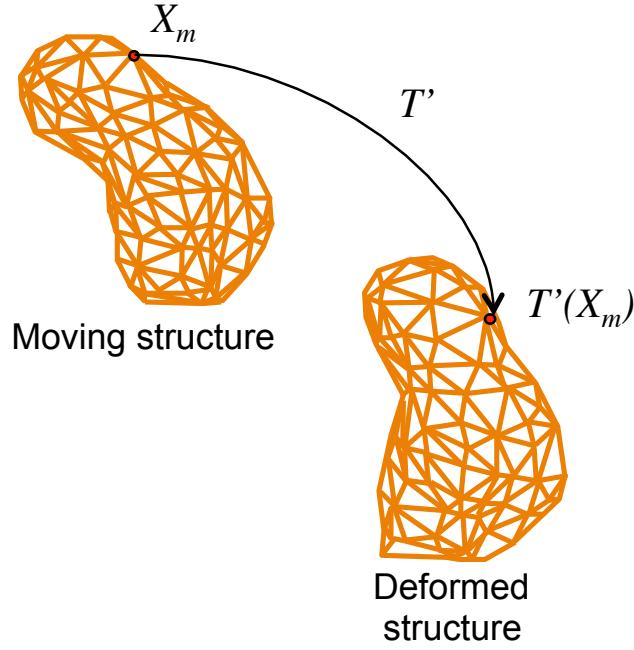


Figure 3.7: Organ structure from moving image to deformed structure.

$$C = \frac{1}{N_1} \sum_{l=1}^{N_1} (I_M(T(\mathbf{x}_l)) - I_F(\mathbf{x}_l))^2 + \alpha \frac{1}{N_2} \sum_{m=1}^{N_2} \sum_{n=1}^{n(\mathbf{Z}_m)} (I_M(\mathbf{z}_n) - I_M(T'(\mathbf{X}_m)))^2 \quad (3.16)$$

In both Figure 3.7 and Equation (3.16),  $\mathbf{X}_m$  represents node position in uterus structure,  $N_1$  and  $N_2$  are the normalization factors corresponding to the number of voxels and structure nodes respectively, and  $\alpha$  is the weight of biomechanical term in cost function. Here,  $\mathbf{Z}_m = \{\mathbf{x} \mid \|T(\mathbf{x}) - T'(\mathbf{X}_m)\| < d\}$  with  $d$  is a specified threshold and  $\mathbf{z}_n \in \mathbf{Z}_m$ .  $T$  is the free-form deformation based on B-splines, which is transformation model used in intensity-based registration. Intensity-based registration, along with other registration

components used in the experiment will be explained in Section 3.3.  $T'$  is deformation coming from biomechanical simulation with finite element analysis, which will be explained in Section 3.4. The second term in this extended cost function has similar function with the SSD metric, except that it uses intensity corresponds to organ structure after simulation rather than intensity from the fixed image in order to include the effect of physical deformation in it.

### Transformation Model

The combined registration is done based on intensity using parametric approach after biomechanical simulation result is included in it. Transformation model is used to relate the moving image and the fixed image in registration process. Due to anisotropic nature of clinical image with large deformation in target organ, rigid transformation which only represents global transformation in image is not enough to deform the moving image to match the fixed image. Free-form deformation (FFD) based on B-splines [26, 27] is used as non-rigid transformation to model local deformation in image.

$$\begin{aligned}
B_0(r) &= (1 - r)^3/6 \\
B_1(r) &= (3r^3 - 6r^2 + 4)/6 \\
B_2(r) &= (-3r^3 + 3r^2 + 3r + 1)/6 \\
B_3(r) &= r^3/6
\end{aligned} \tag{3.17}$$

In Equation (3.17),  $B_q$  are the  $q^{th}$  basis function to define cubic B-splines where  $0 \leq r < 1$ . By using these functions, transformation function  $T(x, y, z)$  for image volume  $\Omega = \{(x, y, z) | 0 \leq x < V_x, 0 \leq y < V_y, 0 \leq z < V_z\}$  can be written as Equation (3.18). This transformation is locally controlled by  $n_x \times n_y \times n_z$  grid of control points  $\phi_{i,j,k}$  with uniform spacing.

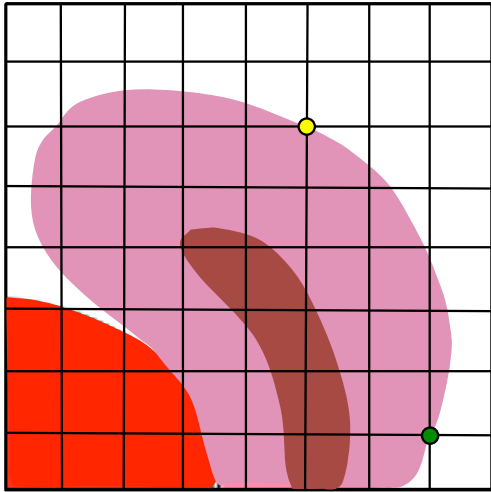
$$T(x, y, z) = \sum_{l=0}^3 \sum_{m=0}^3 \sum_{n=0}^3 B_l(r) B_m(v) B_n(w) \phi_{i+l, j+m, k+n} \tag{3.18}$$

where  $i = \lfloor x/n_x \rfloor - 1$ ,  $j = \lfloor y/n_y \rfloor - 1$ ,  $k = \lfloor z/n_z \rfloor - 1$ ,  $r = x/n_x - \lfloor x/n_x \rfloor$ ,  $v = y/n_y - \lfloor y/n_y \rfloor$ ,  $w = z/n_z - \lfloor z/n_z \rfloor$  and  $B_l(r)$ ,  $B_m(v)$ , and  $B_n(w)$  represents cubic

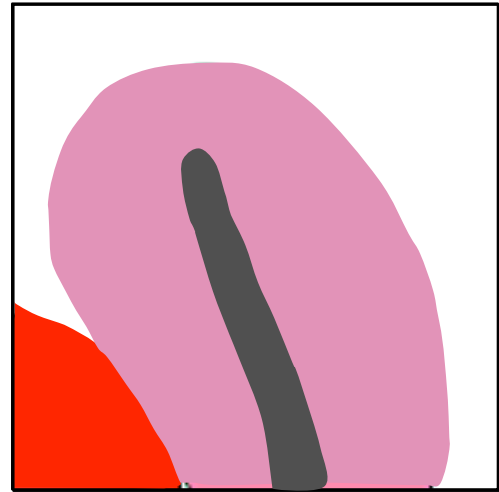
B-spline basis function evaluated at  $r$ ,  $v$  and  $w$ , respectively. Here, operator  $\lfloor \cdot \rfloor$  denotes the floor function to obtain integer that represents the nearest grid from coordinate  $x$ ,  $y$  or  $z$  in image.

The idea of this free-form deformation is to deform object in image by manipulating an underlying mesh of control points [26]. By changing control point  $\phi_{i,j,k}$ , 8 voxels that share the control point in its local neighborhood will be affected. It means, when a control point is moved, only area surrounding that point will be transformed, thus enabling local deformation in certain area in image. In addition, setting the grid spacing to a smaller size increases the number of parameter (degree of freedom) and provides a more flexible adjustment of control points. Therefore, it allows modeling of highly local non-rigid deformations.

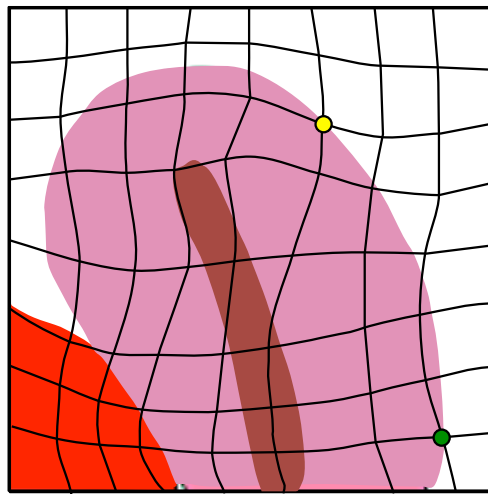
Figure 3.8 illustrates the free-form deformation based on B-splines. Figure 3.8(a) represents the moving image, Figure 3.8(b) represents the fixed image, and Figure 3.8(c) represents the deformed moving image. Yellow and green dots in these figures show samples of corresponding control point in image before and after transformation. It is shown that free-form deformation model allows deformations only in certain areas in image by manipulating grid of control points.



(a) ROI from moving image



(b) ROI from fixed image



(c) Deformed moving image

Figure 3.8: Free-form deformation based on B-splines.

## Multi-resolution Strategy

To obtain better registration performance in term of transformation model and computational cost, hierarchical multi-resolution approach [28] is applied in the registration process. The strategy is done by gradually changing the transformation model complexity. Registration process is divided into several resolutions. For each resolution, different grid spacing for control points in transformation model is configured.

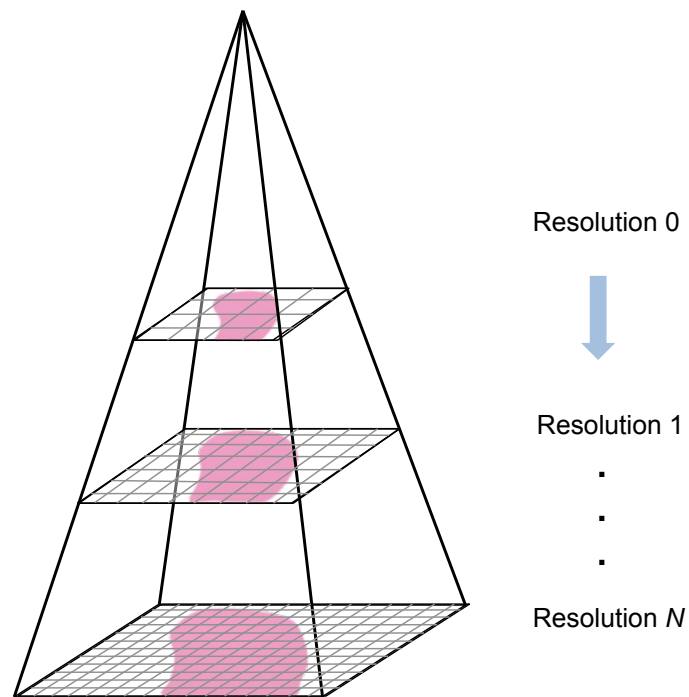


Figure 3.9: Multi-resolution strategy.

Figure 3.9 illustrates example of image data representation in three level resolutions strategy. The grid spacing is set to be coarse in the very first resolution, and then it is refined in the subsequent resolutions. By applying this strategy, there will be reduction of information content within the images to be matched. Therefore at first, only the coarsest and most global structures remain in the image. Refinement in grid spacing size gradually defines more detailed structure of image, thus improving the optimization process of image registration. This method can also provide a way to reduce memory overload when a large data set is used in registration [29].

# Chapter 4 Image Registration and Biomechanical Simulation as an Integrated Process

## 4.1 Material and Data

The developed deformable image registration method is experimented on a pair of X-ray CT scan of woman's pelvis phantom and five pairs of clinical images from five different patients taken during radiation treatment. The following sub-sections describe the properties of these images.

### 4.1.1 Phantom Data

Phantom is made to have similar shape and anatomy with the real woman pelvis. It consists of artificial pelvis organs including bladder, uterus and rectum. The uterus in this phantom is made of urethane with markers placed on several locations of this phantom. Structure data of uterus segmented by radiation oncologist is included in the image set.

Figure 4.1 shows the actual phantom that is used to obtain phantom images. There are two versions of X-ray CT scan of phantom, one is the raw image set with plastic body as well as the space inside uterus visible, while the other has image processing applied to it to remove the body of the phantom and correct the intensity inside uterus to mimic the actual clinical data. Figure 4.2, 4.3 and 4.4 shows axial, coronal, and sagittal view of original X-ray CT scan of pelvis phantom during insertion and non-insertion of radiotherapy applicator, respectively. In these figures, uterus as target organ is indicated with yellow line. In the experiment, the image during insertion of applicator will be used as fixed image, while the other one will be used as moving image.

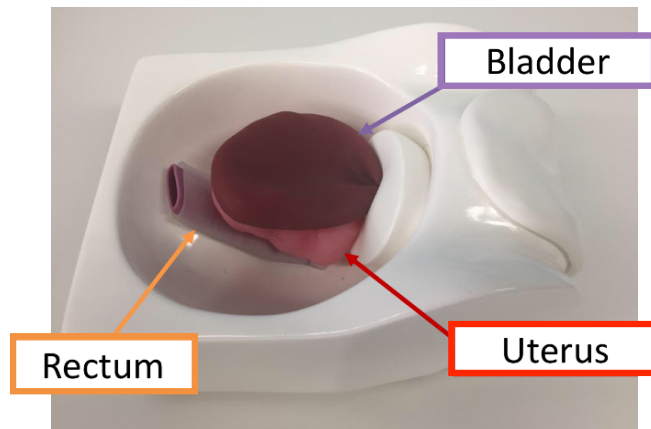
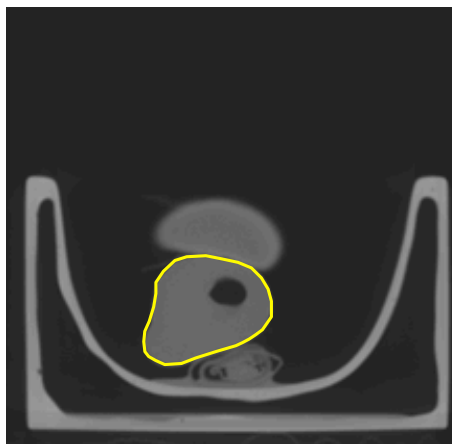
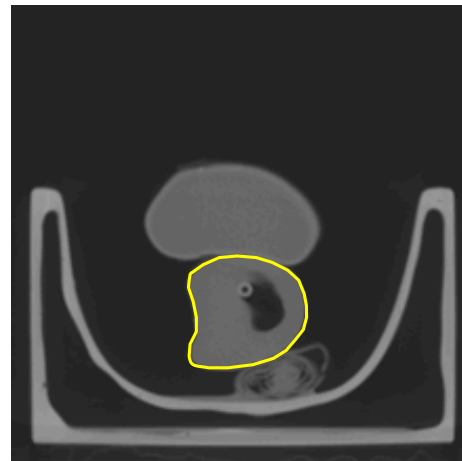


Figure 4.1: Woman pelvic phantom used to obtain phantom images.

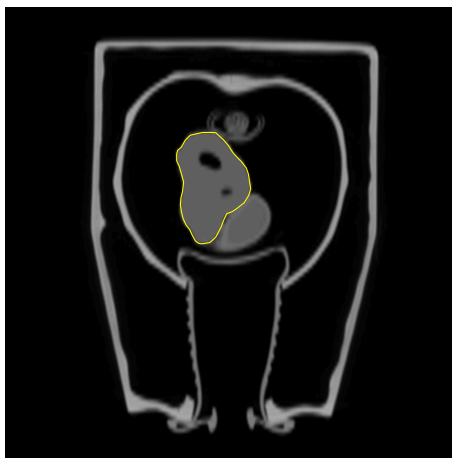


(a) Moving image

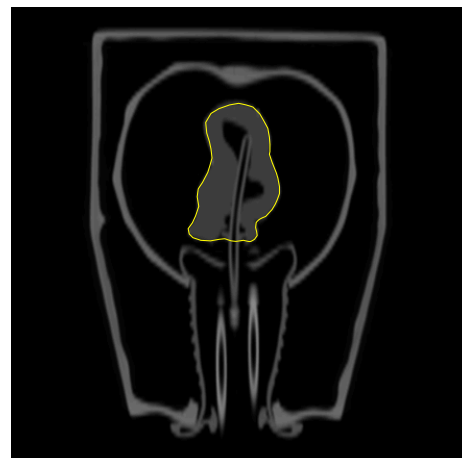


(b) Fixed image

Figure 4.2: Axial view of phantom images.



(a) Moving image



(b) Fixed image

Figure 4.3: Coronal view of phantom images.

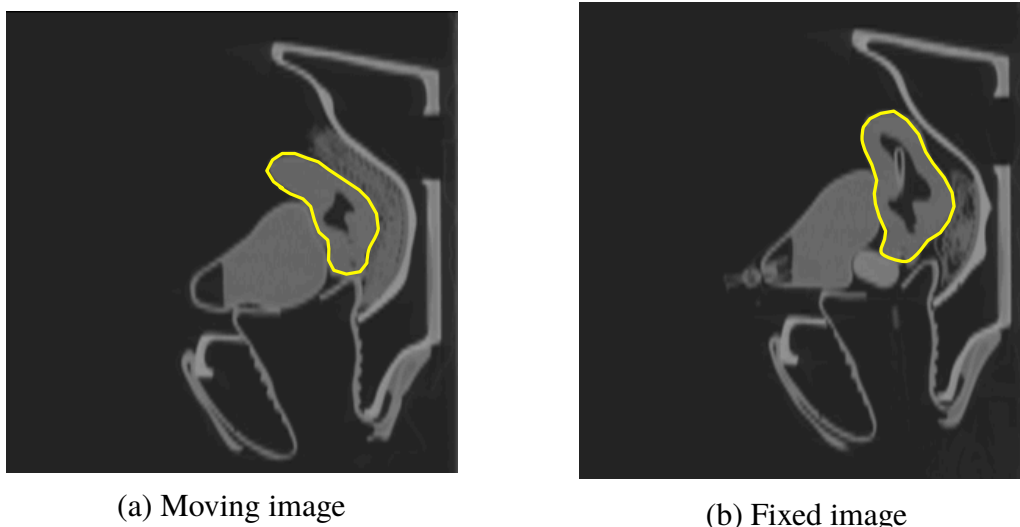


Figure 4.4: Sagittal view of phantom images.

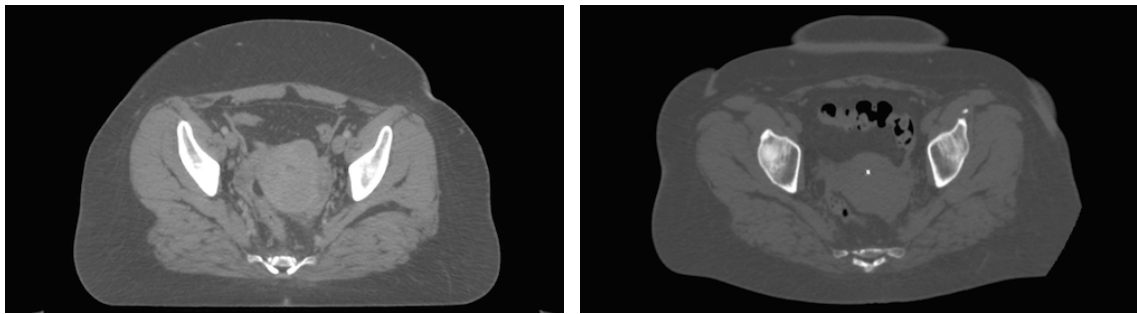
Table 4.1 shows the properties of phantom images used in the experiment.

Table 4.1: Properties of phantom images.

Input images		Image size	Voxel size [mm]
Type	Moving image	$512 \times 512 \times 152$	$0.781 \times 0.781 \times 2.500$
	Fixed image	$512 \times 512 \times 152$	$0.781 \times 0.781 \times 2.500$

### 4.1.2 Clinical Data

X-ray CT scans of patient's pelvic area are taken during external beam radiotherapy (EBRT) and intracavitary brachytherapy (ICBT) for cervical cancer treatment. In ICBT image, target organ (uterus) is largely deformed due to insertion of plastic applicator used in treatment. EBRT image serves as moving image, and ICBT image serves as fixed image. These image sets come from five different patients P4, P5, P6, P7 and P8, all with the size of  $512 \times 512$  pixels. The number of slices for EBRT images are 189, 141, 197, 169, and 153, while ICBT images have 118, 114, 111, 128, and 112 slices, respectively. Overall pixel size of input image is  $0.977 \text{ mm} \times 0.977 \text{ mm}$  with slice thickness of 2.5 mm for EBRT image and 2 mm for ICBT image. In the experiment, EBRT image will be deformed to be spatially aligned with ICBT image. Figure 4.5, 4.6 and 4.7 show axial, coronal, and sagittal view of the CT X-ray images from one of the patients (P6), respectively, and Table 4.2 shows its properties.



(a) Moving image

(b) Fixed image

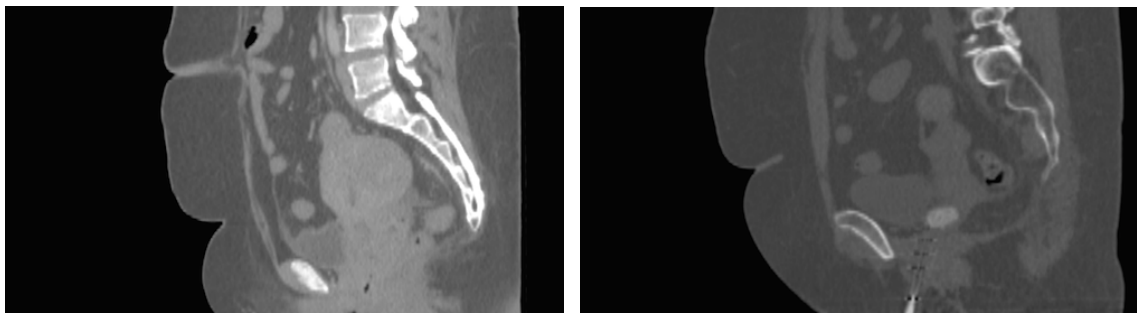
Figure 4.5: Axial view of clinical images.



(a) Moving image

(b) Fixed image

Figure 4.6: Coronal view of clinical images.



(a) Moving image

(b) Fixed image

Figure 4.7: Sagittal view of clinical images.

Table 4.2: Properties of clinical images.

Input images		Image size	Voxel size [mm]
Type	Moving image	$512 \times 512 \times 197$	$1.172 \times 1.172 \times 2.500$
	Fixed image	$512 \times 512 \times 111$	$0.977 \times 0.977 \times 2.000$

The clinical image set also has structure data of target organ, segmented by radiation oncologist beforehand. Structure information will be used in volume reconstruction of target organ as well as in evaluation of image registration result to see performance of registration process in handling internal anatomy. Figure 4.8 shows axial view of input images with target organ (uterus) indicated on it. In Figure 4.8(a), uterus is indicated with orange line, and in Figure 4.8(b), uterus is indicated with blue line. Figure 4.9(a) and Figure 4.9(b) shows three dimensional visualization of segmented target organ (uterus) surface from moving image and fixed image, respectively.

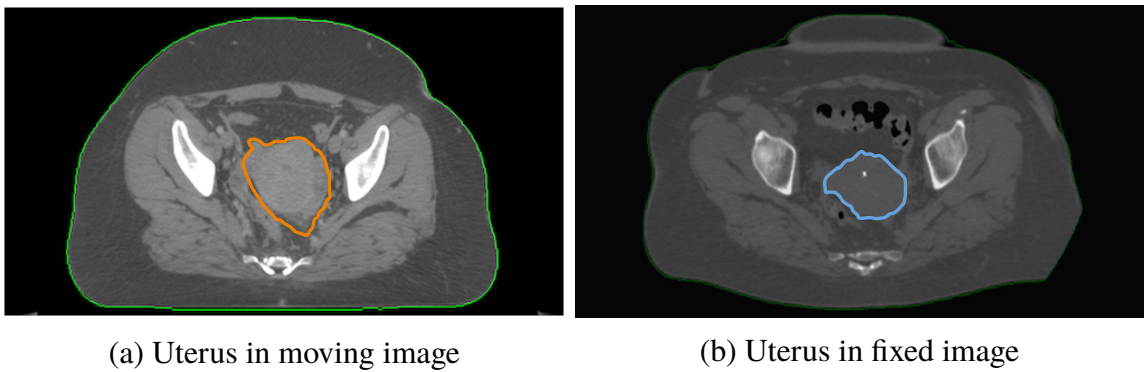


Figure 4.8: Segmented target organ in clinical images.

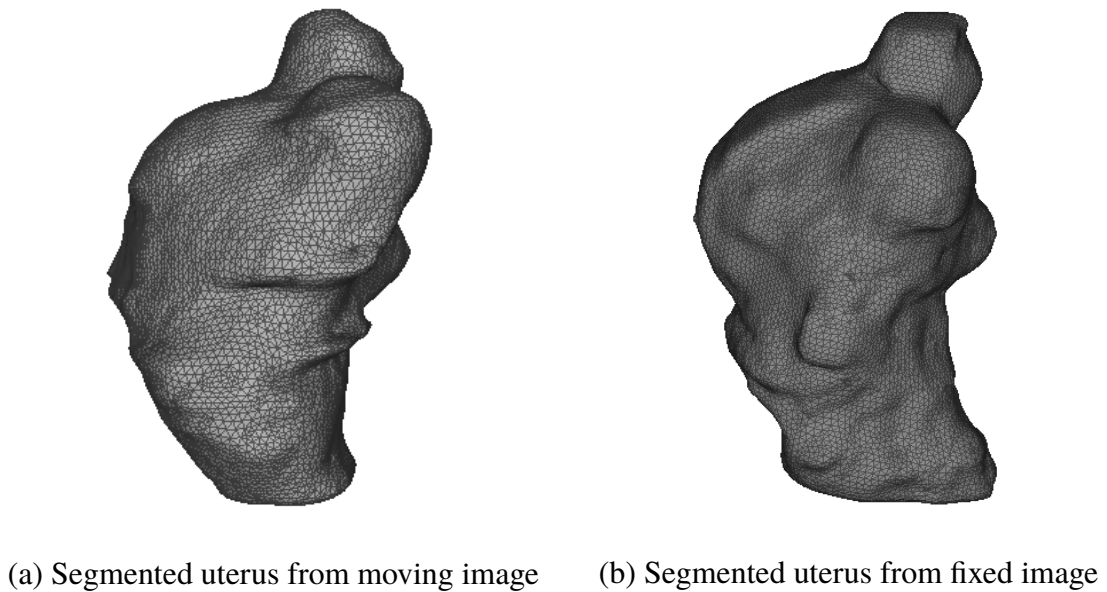


Figure 4.9: Three dimensional visualization of segmented target organ.

## 4.2 Experiment

Preliminary experiment is done by manually selecting corresponding points whose distance is used as displacement boundary condition in biomechanical simulation. The corresponding point is selected by observing intensity similarity between tip of applicator from fixed image and tip of internal wall of uterus from moving image. In this experiment, the original X-ray CT scan of phantom without correction is used. Figure 4.10 shows the corresponding point selection on the phantom image. In Figure 4.10(b), applicator inside uterus is highlighted with blue line and the selected corresponding point is marked in yellow.

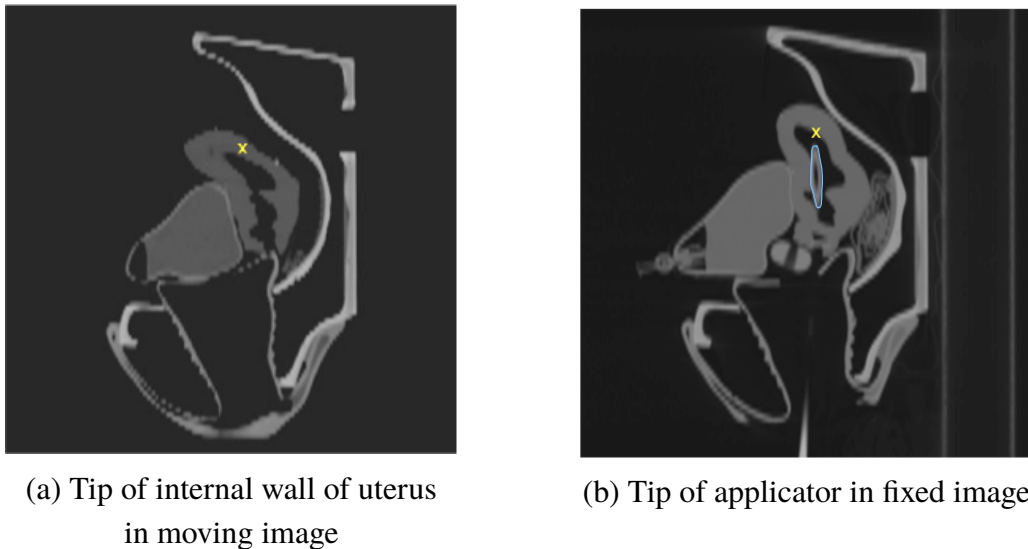


Figure 4.10: Corresponding point selection in preliminary experiment.

This preliminary experiment with manual selection of corresponding point will then be improved by performing object skeletonization as a way to obtain corresponding points between images automatically.

For all experiments, volumetric meshing for uterus structure is done by Amira software, preprocessing, centerline detection and finite element analysis are performed on MATLAB and the combined registration is performed on Elastix [30] platform. Figure 4.11 shows phantom uterus structure taken from moving image that is used in preliminary biomechanical simulation in posterior-superior direction.

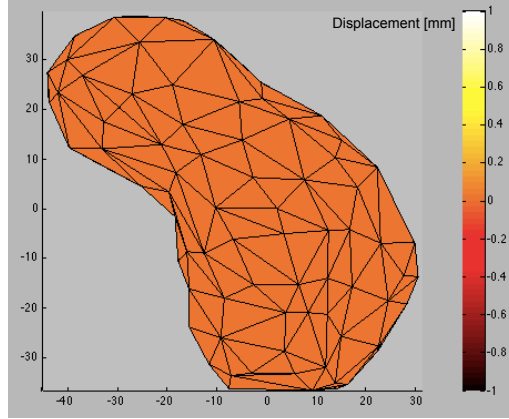


Figure 4.11: Uterus model before simulation.

Table 4.3 shows properties assigned in biomechanical simulation, Table 4.4 shows registration parameter configuration, and Table 4.5 shows specification of PC used to do biomechanical simulation in this experiment. Parameter that is used to configure registration process including grid spacing and iteration times are selected within the range of recommended value in Elastix configuration. There are various researches that perform tension tests on human uterus tissue to obtain its material properties, one of them is reported in [31]. The simulation in this experiment uses averaged material properties for uterus tissue stated in [32], whose value is also used for finite element analysis in [33].

Table 4.3: Properties for simulation.

Parameter	Phantom image	Clinical image
Young's Modulus	4.5 MPa	566 kPa [32]
Poisson's Ratio	0.45	0.4
Number of element	551	3135 to 3821

Table 4.4: Registration configuration.

Grid spacing [mm]				Number of iterations per resolution	
R0	R1	R2	R3	Phantom image	Clinical image
20	10	5	2.5	500	1000

Table 4.5: PC specification.

OS	Windows 7 Professional
CPU	Intel Core i7-950 3.07 GHz
RAM	24.0 GB

## 4.3 Result and Evaluation

### 4.3.1 Evaluation Method

Results of the experiments with the combined registration method are compared with the results from other original methods. These results are evaluated qualitatively by manual inspection as well as quantitatively by several parameters. The following sub-sections describe several evaluation method used to assess the performance of registration method.

#### Dice Computation

For two overlapping regions, dice similarity coefficient (DSC) is defined as the ratio of the number in the intersection to the mean label volume [34]. In the evaluation of intensity-based image registration, particularly, in term of internal anatomical structures, DSC value is commonly computed to measure the overlap between certain organ after registration with the desired shape of organ. DSC is computed based on Equation (4.1).

$$DSC(O_1, O_2) = \frac{2|O_1 \cap O_2|}{|O_1| + |O_2|} \quad (4.1)$$

where  $DSC$  is the DSC value,  $O_1$  and  $O_2$  represent the binary label images of organ which similarity is to be calculated,  $| \cdot |$  denotes the number of voxels with the value of 1, and  $\cap$  denotes the intersection of  $O_1$  and  $O_2$ , which is a set of voxels in  $O_1$  that also belong to  $O_2$ . A value of 1 indicates a perfect match between the shape of organ obtained from registration result and target shape, while a value of 0 indicates there is no overlap at all between the two shape of organs. It means, in the range of 0 and 1, the higher DSC value, the better correspondence between organ shape. Figure 4.12 illustrates the DSC for different cases of organ overlap.

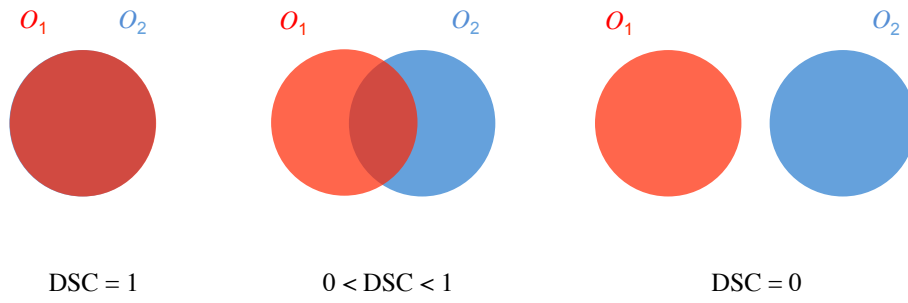


Figure 4.12: DSC as a measurement of spatial overlap.

### Hausdorff Distance

Hausdorff distance measures the degree of mismatch between two point sets. In comparing organ in volumetric images, these point sets are the points on surface of organ model. Hausdorff distance is defined as [35]

$$HD(O_a, O_b) = \max(h(O_a, O_b), h(O_b, O_a)) \quad (4.2)$$

where  $h(O_a, O_b) = \max_a \min_b \|a - b\|$ ,  $O_a$  and  $O_b$  each is a set of points that represents surface of organ model,  $a$  is element of  $O_a$  and  $b$  is element of  $O_b$ . Figure 4.13 illustrates the hausdorff distance between organ two surfaces of organ.

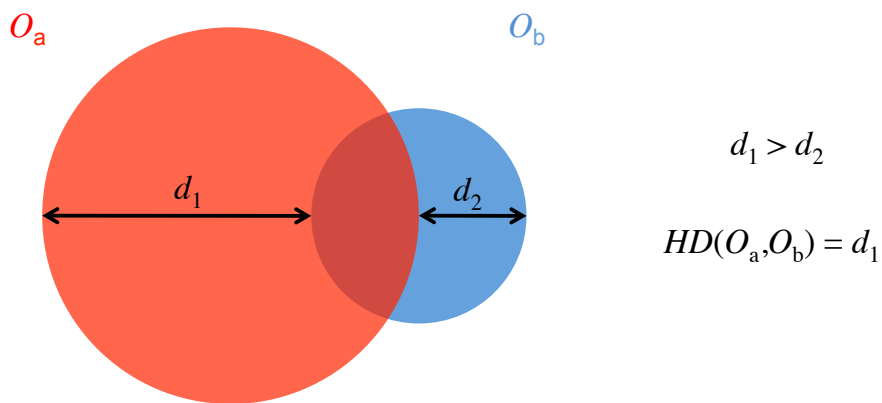


Figure 4.13: Hausdorff distance in image matching.

Supposed that  $h(O_a, O_b)$  is in a value of  $d_1$  and  $h(O_b, O_a)$  is  $d_2$  and  $d_1 > d_2$ , hausdorff distance between  $O_a$  and  $O_b$  is  $d_1$ .

## Demon Algorithm

Demons algorithm [21] is one of the most widely used algorithms in deformable image registration. It is also often used as a standard performance comparison for new developed framework. This method is based on optical flow to find small deformations in sequences of images.

Figure 4.14 shows how displacement is estimated from moving image to fixed image. For a given point P in the image,  $f$  is the intensity function in the fixed image and  $m$  is the intensity in the moving image. In optical flow, intensity of the moving image is considered to be constant, which gives optical flow equation as seen in Equation (4.3) for small (unity) step of intensity in fixed image.

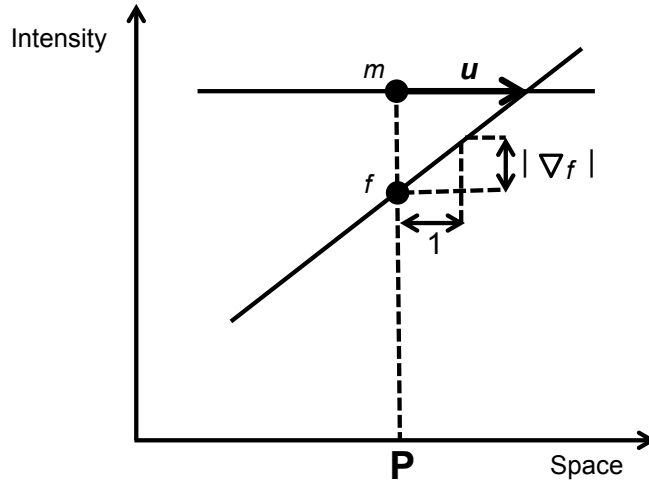


Figure 4.14: Displacement estimation from moving image to fixed image.

$$\mathbf{u} \cdot \nabla_f = m - f \quad (4.3)$$

Based on this, arranging the equation and adding the term  $(m - f)^2$  to provide stability in the equation, estimated displacement  $\mathbf{u}$  required for point P in fixed image to match the corresponding point in the moving image in demons algorithm is calculated by Equation (4.4).

$$\mathbf{u} = \frac{(m - f) \nabla_f}{|\nabla_f|^2 + (m - f)^2} \quad (4.4)$$

where  $\mathbf{u} = (u_x, u_y, u_z)$  in 3D and  $\nabla_f$  is gradient of the fixed image.

### 4.3.2 Combined Registration with Manually Selected Corresponding Point

Figure 4.15 shows deformed uterus structure after finite element analysis with the given displacement constraint from the manually selected corresponding point in left-posterior, left-superior and posterior-superior view in comparison to those of structure from fixed image in Figure 4.16. Colorbars in these figures show the displacement in millimeters.

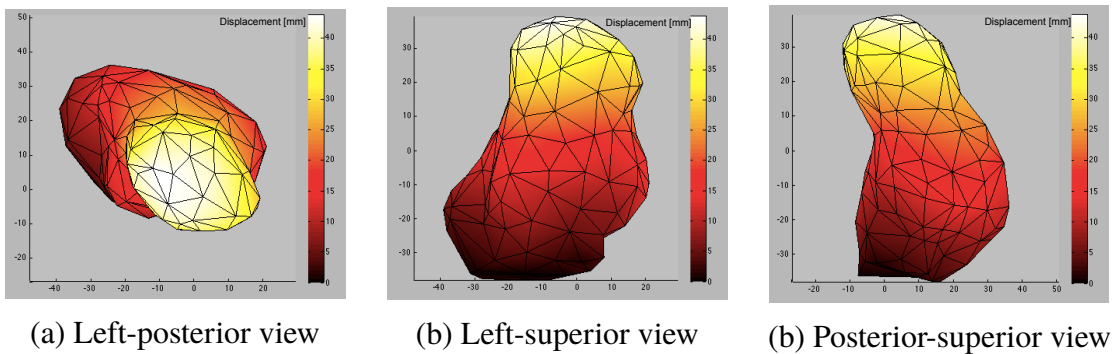


Figure 4.15: Deformed structure of phantom uterus.

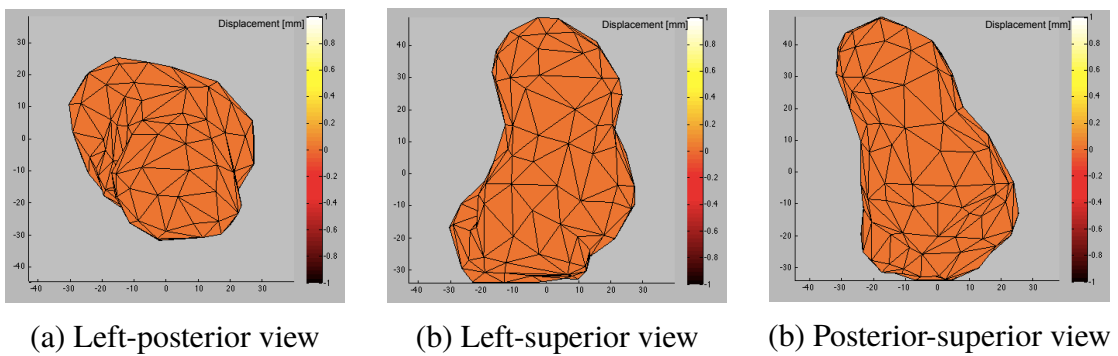
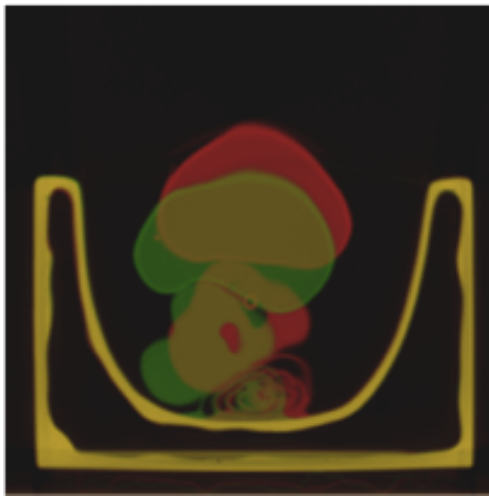


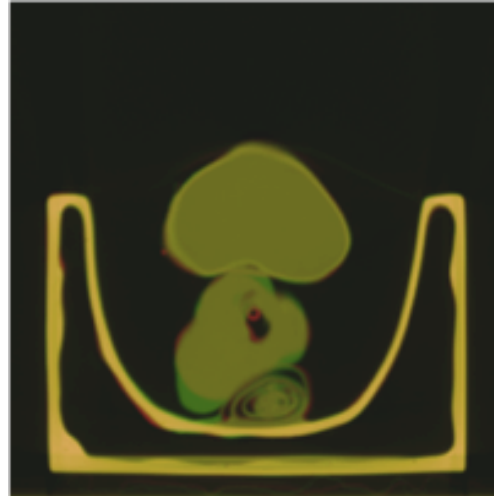
Figure 4.16: Target structure of phantom uterus.

From these figures, it can be observed that the overall uterus structure has been deformed such that it has similar shape and orientation with the structure in fixed image, which means that the assumption of correspondence used in this study is indeed can be used to align the structure to the desired condition.

The previously obtained deformed phantom uterus structure is incorporated into intensity registration to create a combined registration. Figure 4.17 shows superimposed image between fixed and moving images before and after intensity only registration, while Figure 4.18 shows that of before and after combined registration. In these figures, red color shows the fixed image, green color shows the moving image, and yellow color shows the part where fixed and moving images are overlapping or in agreement with each other.

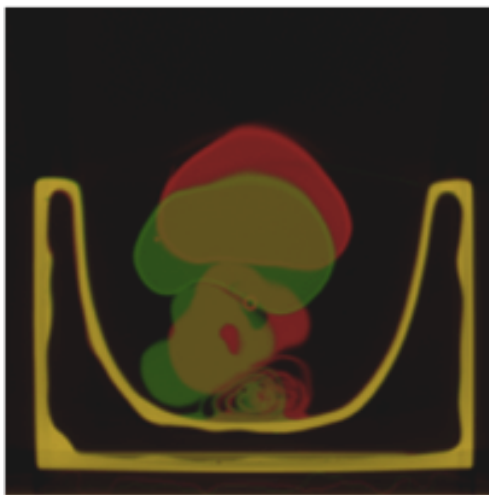


(a) Before registration

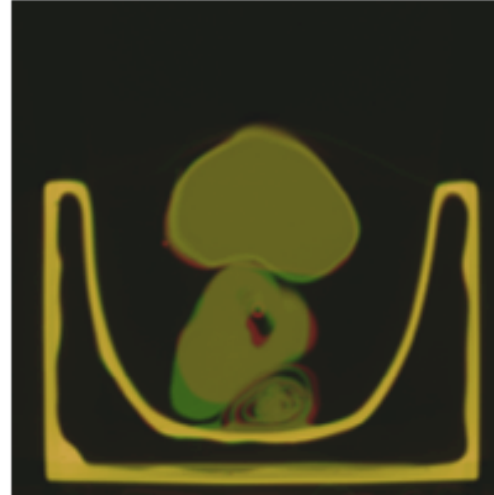


(b) After intensity registration

Figure 4.17: Comparison of phantom image before and after intensity registration.



(a) Before registration



(b) After registration

Figure 4.18: Comparison of phantom image before and after combined registration.

Quantitatively, registration results in Figure 4.17 and 4.18 shows the more overlapping area between fixed and moving images compared to their initial conditions before registration. These images show that intensity-based registration provide non-rigid alignment as the shape of bladder is mostly in agreement to each other. However, the shape of uterus as the organ with physical intervention by radiotherapy applicator still have some non-overlapping regions, proving that the image alignment especially in correlation with anatomical variation by intensity-based only registration is not enough.

After the addition of biomechanical term, the way shape of uterus change is different compared to that of intensity-only registration, even though it also still does not give perfect overlap. These slight difference can be observed from uterus area in Figure 4.17(b) and 4.18(b). Here from the axial (left-posterior) view, the uterus in registration result for combined method has slightly longer shape and non-overlapping area in along the posterior direction, while the registration result for intensity-only registration has slightly more non-overlapping area in left direction.

To complement the evaluation of registration result based on visual inspection, further evaluation on this registration is done quantitatively by comparing several marker locations in the fixed image, original moving image, and images after intensity as well as combined registration. In this experiment, three markers  $mp_0$ ,  $mp_1$  and  $mp_2$  are used in the evaluation. Localization of these marker positions are done by manual inspection according to intensity in surrounding organ from sagittal, axial and coronal view, respectively.

Figure 4.19, 4.20, and 4.21 shows marker locations used in evaluation process and Table 4.6, 4.7, and 4.8 shows the corresponding comparison between target and registration result for each of three sample marker, respectively.

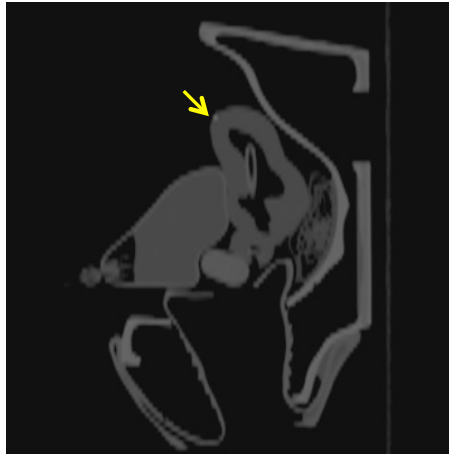


Figure 4.19: Marker  $mp_0$  from sagittal view.

Table 4.6: Location comparison for marker  $mp_0$ .

Image	Position [mm]		
	Left	Posterior	Superior
Fixed	6.250	-30.042	42.605
Moving	-12.500	-44.103	26.710
Intensity registration result	0.781	-32.487	37.103
Combined registration result	1.563	-32.962	37.159

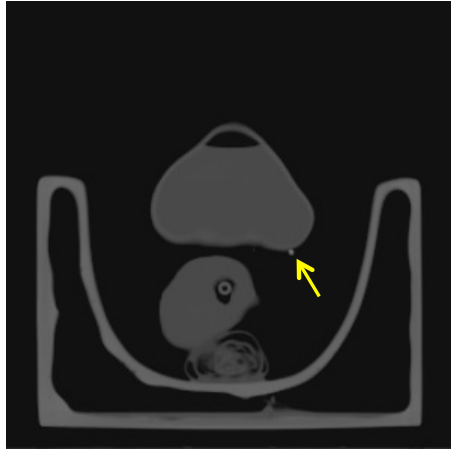


Figure 4.20: Marker  $mp_1$  from sagittal view.

Table 4.7: Location comparison for marker  $mp_1$ .

Image	Position [mm]		
	Left	Posterior	Superior
Fixed	30.483	-25.762	-25.000
Moving	26.815	-12.312	-27.500
Intensity registration result	32.318	-27.596	-27.500
Combined registration result	31.501	-27.001	-27.500



Figure 4.21: Marker  $mp_2$  from sagittal view.

Table 4.8: Location comparison for marker  $mp_2$ .

Image	Position [mm]		
	Left	Posterior	Superior
Fixed	-6.199	-5.469	43.217
Moving	-11.089	-6.250	29.155
Intensity registration result	-2.530	-5.469	34.658
Combined registration result	-3.142	-4.689	34.658

By using marker positions shown in the tables, registration accuracy evaluation is done by calculating absolute difference of marker positions in fixed image and registration result for both methods. Average registration error for intensity-only registration is 3.658 mm, 1.426 mm and 5.520 mm in left, posterior and superior directions, respectively, while average registration error for combined registration is 2.921 mm, 1.646 mm and 5.502 mm in left, posterior and superior directions, respectively. It is shown that intensity-only registration result has bigger error in left direction than combined registration result, and combined registration result has bigger error in posterior direction than intensity registration, which might be caused by the non-overlapping regions in Figure 4.17(b) and 4.18(b) explained in the previous qualitative evaluation.

### 4.3.3 Combined Registration using Organ Centerline as Correspondence

Improvement of corresponding point selection is done in the subsequent experiments. Corresponding location between input images are taken from centerline of applicator in the fixed image and centerline of uterus in the moving image, and tip points in these centerline are selected as correspondence. The whole process from image volume pre-processing to the combined registration are experimented on both phantom and patient images. Different from the preliminary experiment explained in the previous section, in this experiment second version of phantom image, which has plastic body removed from it, is used as input.

Figure 4.22 shows the result of reconstructed volume of uterus from moving image and applicator from fixed image from one of patient (P8) and Figure 4.23 shows its respective extracted centerline as series of corresponding points between those volumes. In addition, Figure 4.24 shows uterus and applicator centerlines result from the other patients to show the diversity of uterus shape and orientation between patients.

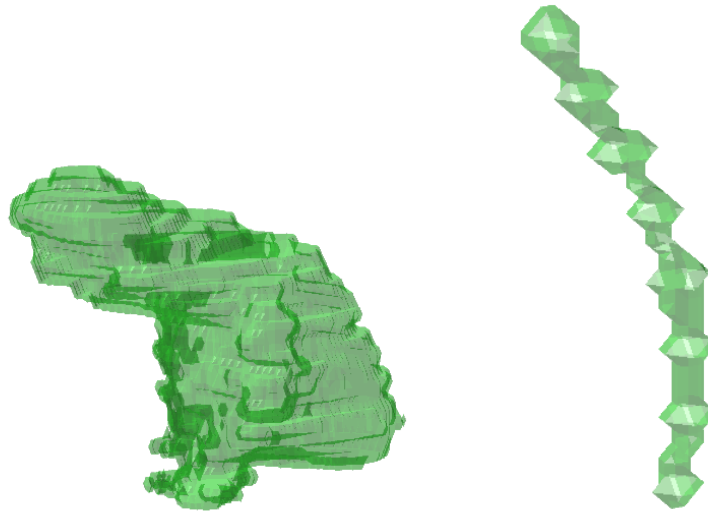


Figure 4.22: Pre-processed volume of uterus(left) and applicator(right) from P8 image pair



Figure 4.23: Extracted centerline of uterus(left) and applicator(right) from P8 image pair

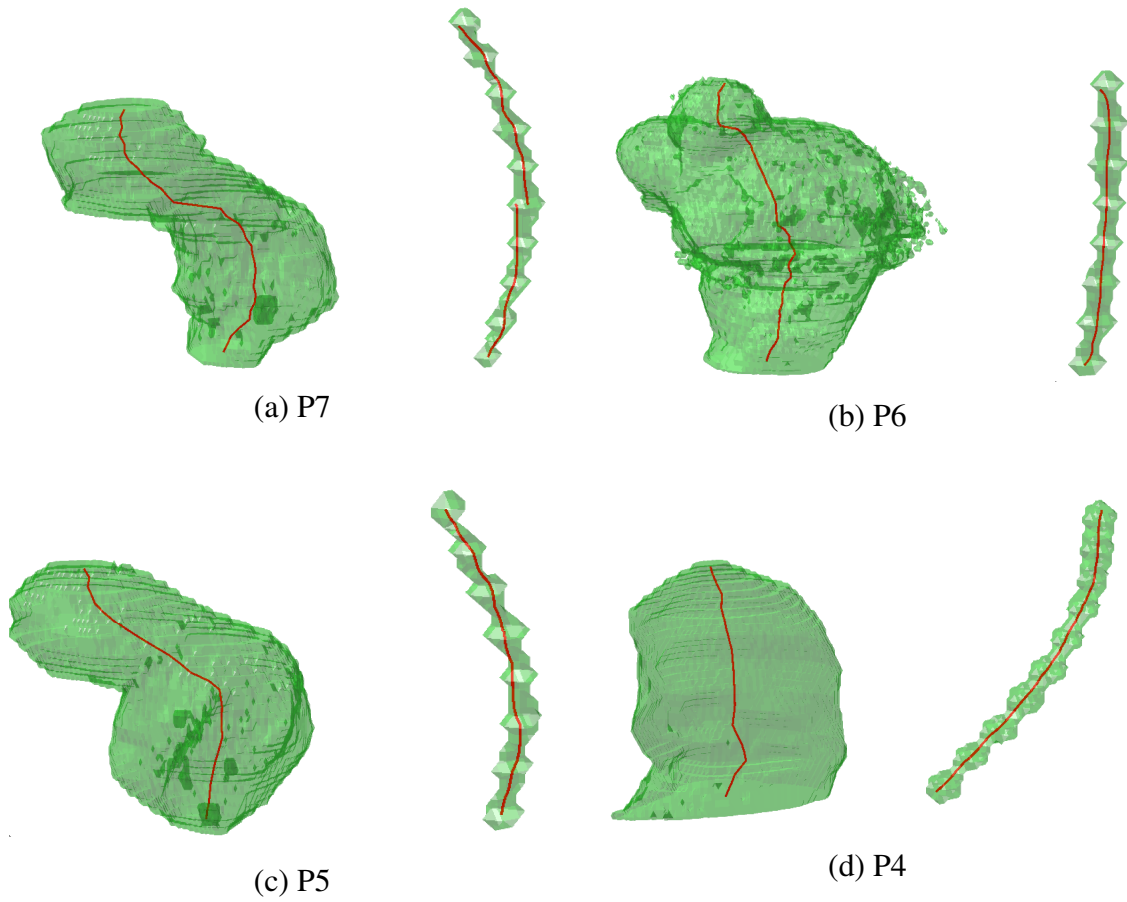


Figure 4.24: Result of extracted centerline from other patient images.

Correspondence between extracted centerline tips is used to calculate displacement boundary condition that will be the input of biomechanical simulation with finite element analysis. Figure 4.25 and 4.26 shows the result of this simulation for patients image whose centerline is extracted in Figure 4.23 for phantom and patient images, respectively.

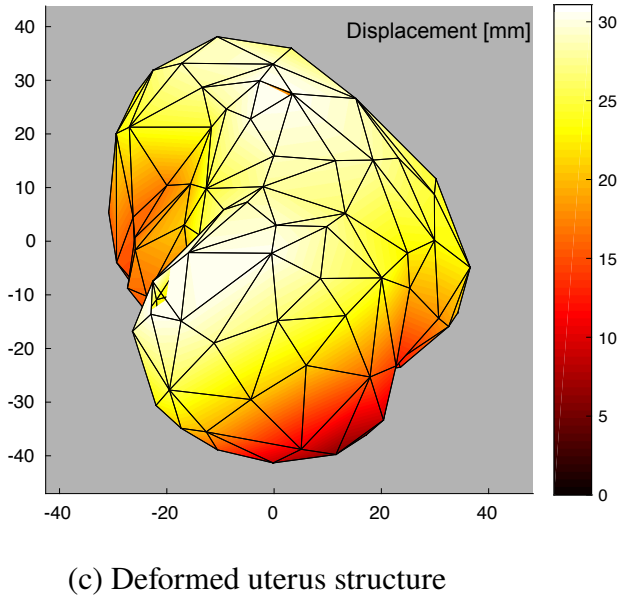
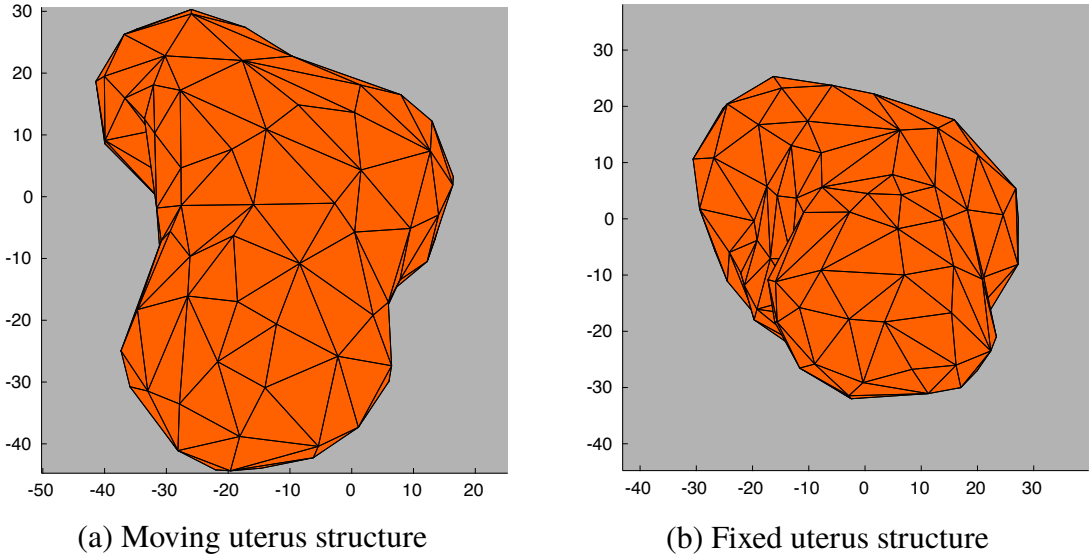
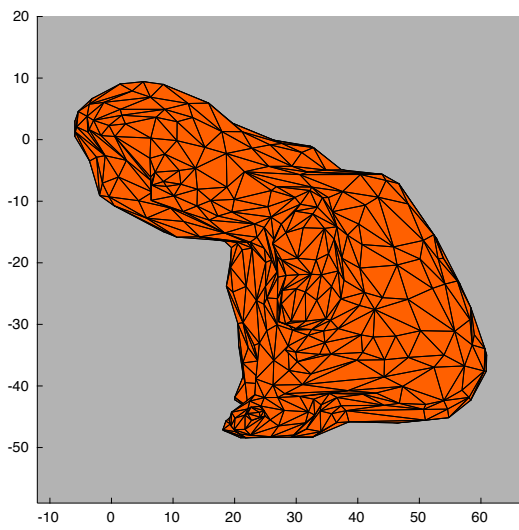
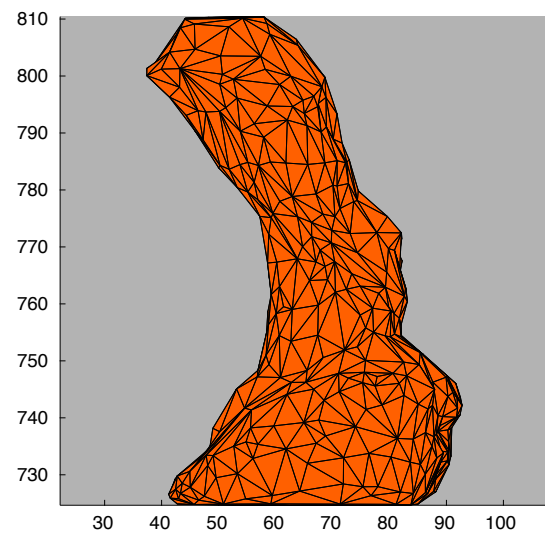


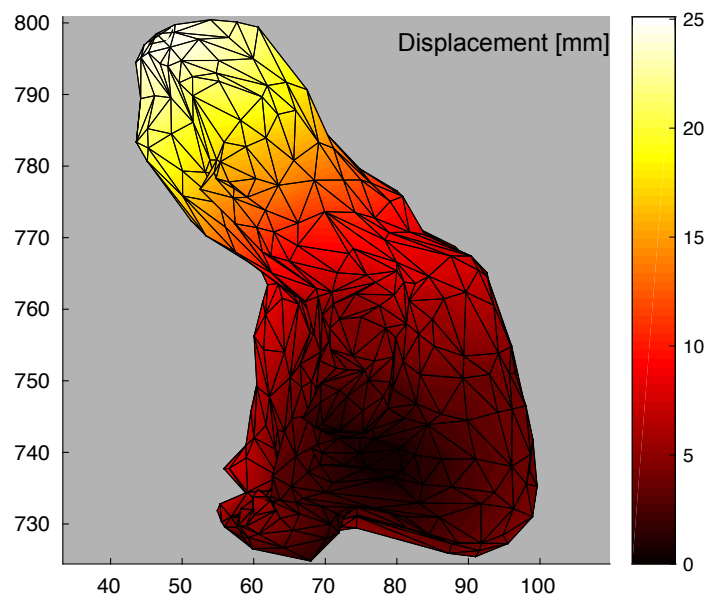
Figure 4.25: Comparison of deformed structure and input image structure from phantom data. Color bar represents displacement in millimeters



(a) Moving uterus structure



(b) Fixed uterus structure



(c) Deformed uterus structure

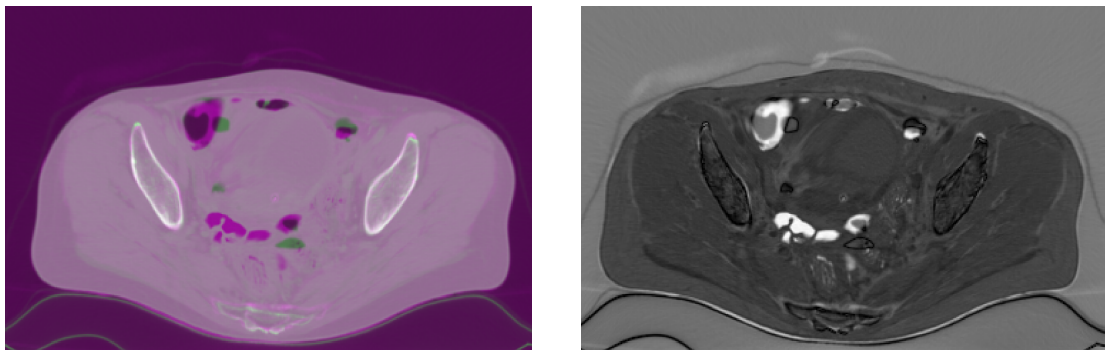
Figure 4.26: Comparison of deformed structure and input image structure from one of patient data. Color bar represents displacement in millimeters

Figure 4.25 shows the volumetric uterus mesh in left-superior view while Figure 4.26 shows uterus mesh in posterior-superior view. In both figures, colormap shows displacement in millimeter unit. Following this process, combined parametric registration is performed to obtain the final deformed image. Figure 4.27 and 4.28 shows the registration result in axial view for phantom and one of patient data, respectively. In Figure 4.27(a) and Figure 4.28(a), magenta color shows the fixed image and green color shows the registration result. If the intensity difference between these images is small and the region is overlapped, white-like color is shown.



(a) Image overlay between registration result and fixed image (b) Difference image between registration result and fixed image

Figure 4.27: Result of combined registration for phantom image



(a) Image overlay between registration result and fixed image (b) Difference image between registration result and fixed image

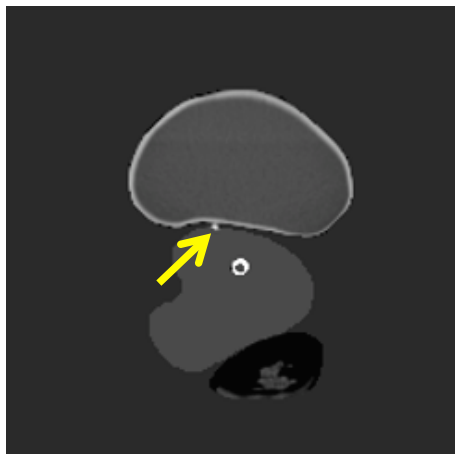
Figure 4.28: Result of combined registration for one of patient image

In Figure 4.27(a) and 4.28(a), regions colored in green and magenta show the intensity difference between registration result and the fixed image. Evaluation done to registration result is different for phantom data and patient data. Different from the previous preliminary experiment, in this experiment, the second version of X-ray CT scan of phantom, which has its plastic body removed, is used. Phantom image has several markers placed on it, which are used to calculate absolute difference between marker locations in fixed image and registration result image.

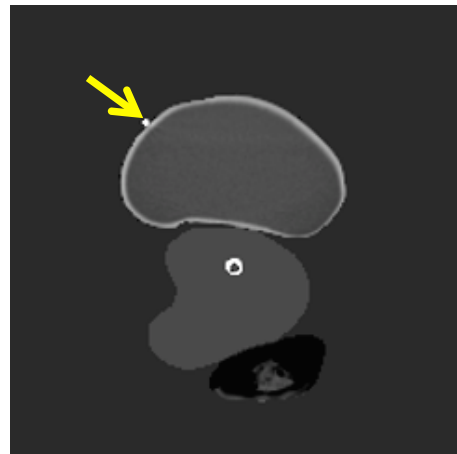
Table 4.9 shows the evaluation result for phantom combined registration in comparison with the intensity-based only registration and Demons algorithm and Figure 4.29 shows the six markers M0, M1, M2, M3, M4 and M5 taken from axial view of the images that are used in this evaluation.

Table 4.9: Evaluation for registration on phantom image.

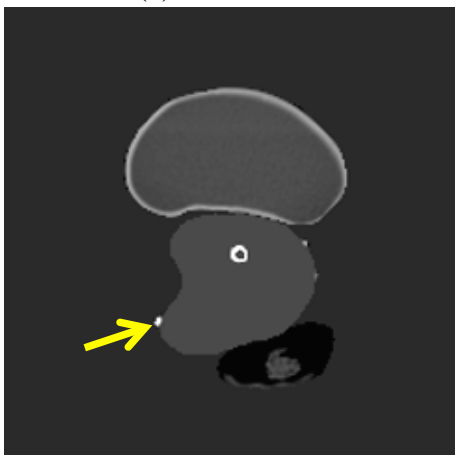
Marker	Method	Registration error [mm]		
		Left	Posterior	Superior
M0	Combined	3.514	4.920	7.5
	Intensity	3.887	6.665	7.5
	Demons	4.809	12.077	7.5
M1	Combined	2.497	0.89	7.5
	Intensity	3.124	2.256	10
	Demons	2.206	5.078	12.5
M2	Combined	2.597	1.076	2.5
	Intensity	5.535	0.271	2.5
	Demons	0.975	4.258	5.0
M3	Combined	3.326	6.322	7.5
	Intensity	2.38	8.134	7.5
	Demons	0.883	8.034	7.5
M4	Combined	2.819	6.896	5
	Intensity	4.215	9.525	2.5
	Demons	1.416	4.583	0
M5	Combined	4.656	1.921	2.5
	Intensity	4.15	4.448	2.5
	Demons	0.398	7.484	7.5



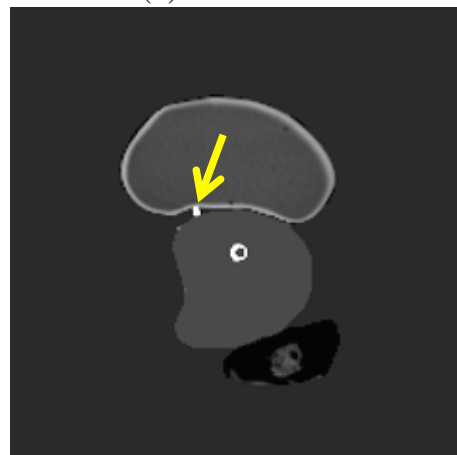
(a) Marker M0



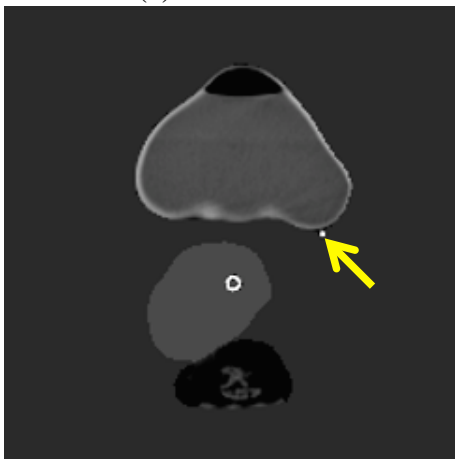
(b) Marker M1



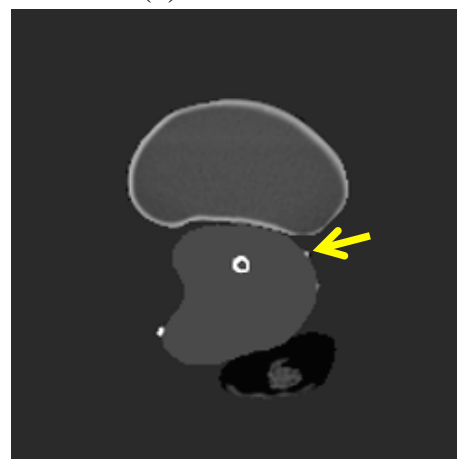
(c) Marker M2



(d) Marker M3



(c) Marker M4



(d) Marker M5

Figure 4.29: Six markers used for the registration evaluation.

Figure 4.30 and 4.31 shows comparison of registration accuracy in each direction and 3D Euclidean, respectively. In both graphs, CM refers to the combined method, I refers to intensity-based only registration and D refers to registration with Demons algorithm.

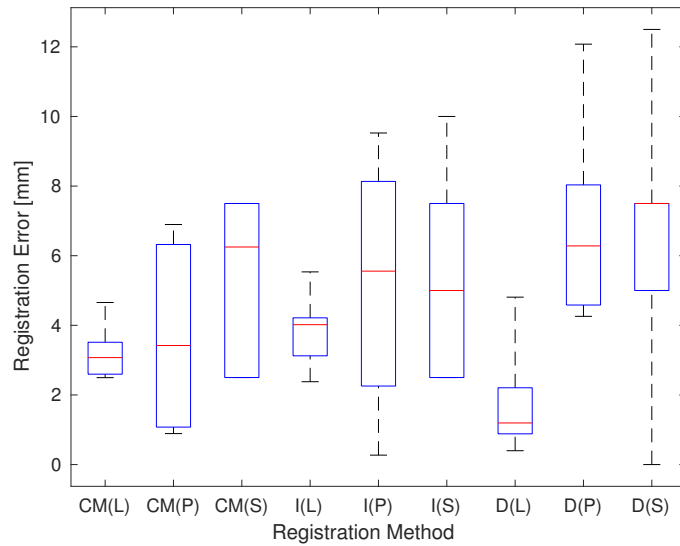


Figure 4.30: Comparison of registration accuracy in all directions

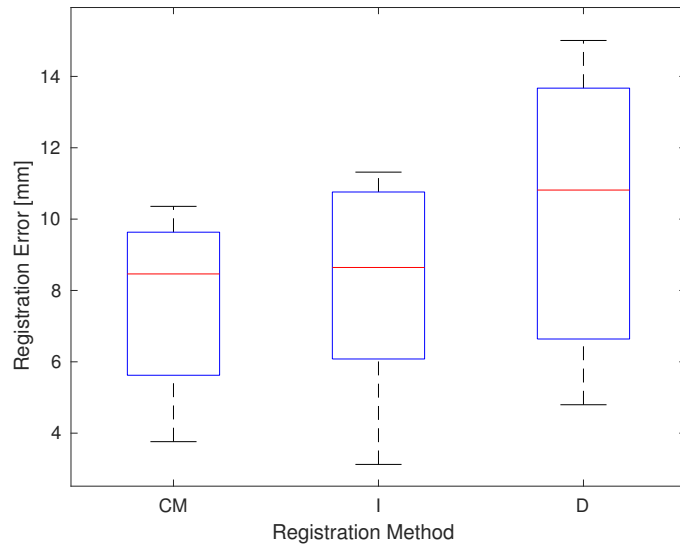


Figure 4.31: Comparison of registration accuracy in 3D Euclidean

The average registration error for combined registration is  $3.235 \pm 0.804$  mm in left direction,  $3.671 \pm 2.703$  in posterior direction,  $5.417 \pm 2.458$  mm in superior direction, and  $7.717 \pm 2.5419$  mm in 3D Euclidean. The average registration error for intensity only

registration is  $3.882 \pm 1.072$  mm in left direction,  $5.217 \pm 3.549$  mm in posterior direction,  $5.417 \pm 3.323$  mm in superior direction, and  $8.095 \pm 3.329$  mm in 3D Euclidean. The average registration error for registration with standard demon algorithm is  $1.781 \pm 1.603$  mm in left direction,  $6.919 \pm 2.970$  mm in posterior direction,  $6.667 \pm 4.083$  mm in superior direction, and  $10.291 \pm 3.945$  mm in 3D Euclidean. This result shows that overall, the combined method with brachytherapy correspondence provide improvement in registration accuracy compared to intensity registration without addition of biomechanical term, even though in comparison with demon algorithm the result still shows a bigger error in left direction.

Evaluation on combined registration for clinical data is done by calculating structure overlap with dice similarity coefficient (DSC) for three organs in pelvic from their segmented binary mask image volume and Hausdorff distance from their surface mesh. Table 4.10 shows the evaluation result for combined registration on clinical data for five pairs of EBRT and ICBT images from five different patients.

Table 4.10: Evaluation for combined registration on patient image.

Subject	Organ	Parameter	
		Hausdorff distance [mm]	Dice similarity coefficient (DSC)
P4	Uterus	30.8	0.578
	Bladder	69.4	0.21
	Rectum	35.8	0.452
P5	Uterus	31.9	0.553
	Bladder	25.8	0.489
	Rectum	20.7	0.546
P6	Uterus	19	0.821
	Bladder	20	0.655
	Rectum	37.1	0.3
P7	Uterus	29.1	0.486
	Bladder	15.5	0.476
	Rectum	25.7	0.345
P8	Uterus	45.8	0.129
	Bladder	25.9	0.722
	Rectum	53.4	0.411

Figure 4.32 and 4.33 shows evaluation of registration with hausdorff distance and DSC, respectively.

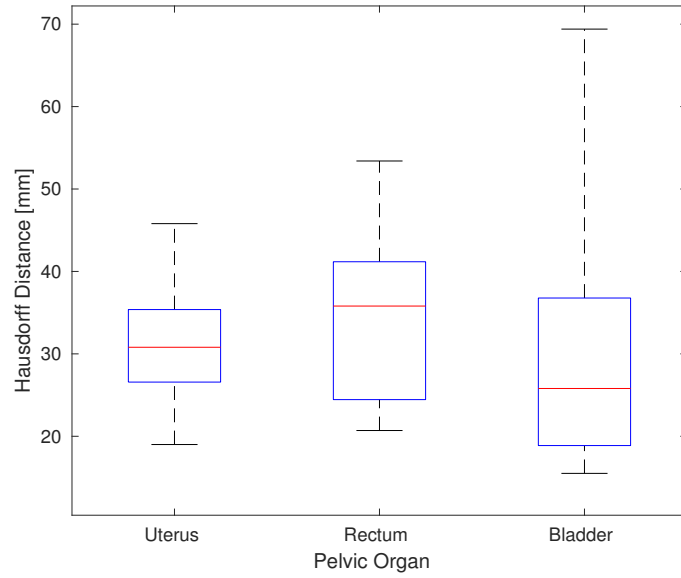


Figure 4.32: Hausdorff distance evaluation for each pelvic organ in clinical data

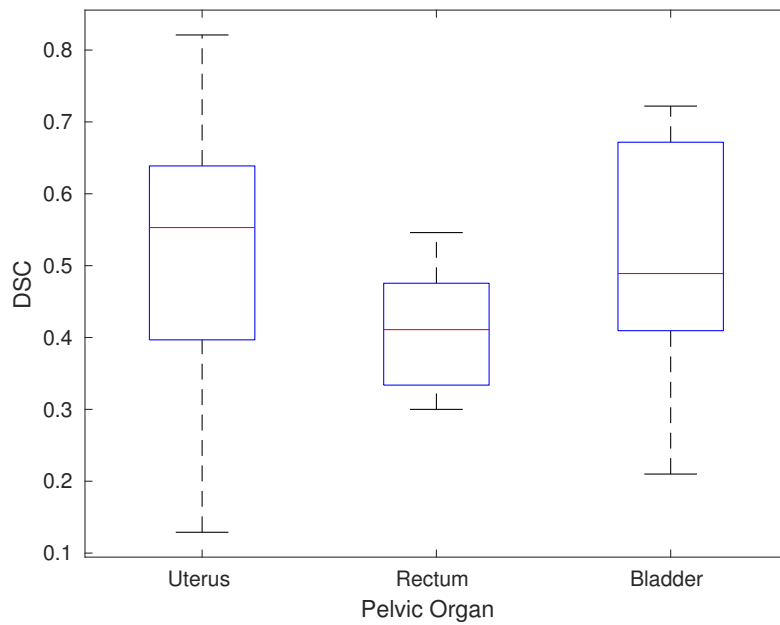


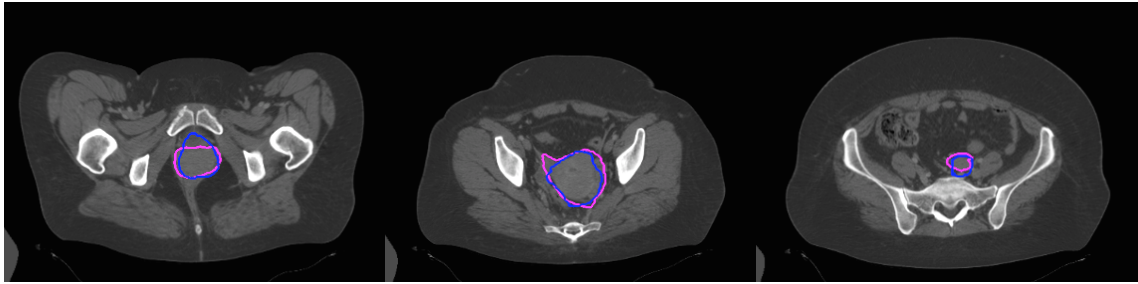
Figure 4.33: DSC evaluation for each pelvic organ in clinical data

The average Hausdorff distance is  $31.32 \pm 8.567$  mm for uterus,  $34.54 \pm 11.256$  mm for rectum and  $31.32 \pm 19.434$  mm for bladder while DSC value is  $0.513 \pm 0.223$  for uterus,  $0.411 \pm 0.085$  for rectum and  $0.510 \pm 0.032$  for bladder. The averaged result gives a rather equal overlapping between the three pelvic organs, however the actual results vary between patients as in some conditions a good overlap (DSC > 0.7) is achieved while in some others the overlap can be lower than 20%.

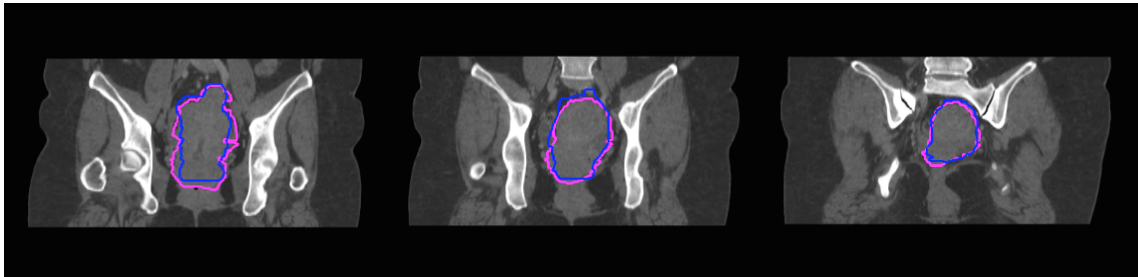
To analyse the variation of registration results in clinical data, visual evaluation is also done to all image pairs, especially the one with good DSC value for uterus (P6 registration) and the one with bad DSC value for uterus (P8 registration). Figure 4.34 and 4.35 shows the good and bad result, each with some sample slices from axial, coronal, and sagittal view. Both of these figures show the deformed image as a result of registration with the combined method overlapped with its corresponding uterus contour and uterus contour from the fixed image, or in other word, the target uterus shape to be match with.

In Figure 4.34, pink line indicates uterus contour corresponds to the deformed image and blue line indicates target uterus contour from the fixed image, while in Figure 4.35, green line indicates uterus contour corresponds to the deformed image and purple line indicates target uterus contour from the fixed image. A good overlap between uterus intensity and target uterus contour can be seen in sagittal view of P6 registration (Figure 4.34), hence the DSC value of 0.821, while the poor match between uterus intensity and target contour that can be seen in P8 registration (Figure 4.35) makes the DSC value of 0.129 understandable.

The other thing that can be observed from these comparison images is that overall lower part of uteri in P6 registration match with each other, while in P8 case, lower part of uteri are quite far apart (uterus in deformed moving images is further to the posterior of patient's body). It shows in P6 case, the non-rigid mismatch between uterus shape is not as big and irregular as the one in P8 case, hence the better organ overlap.



(a) Axial view (interior to superior)

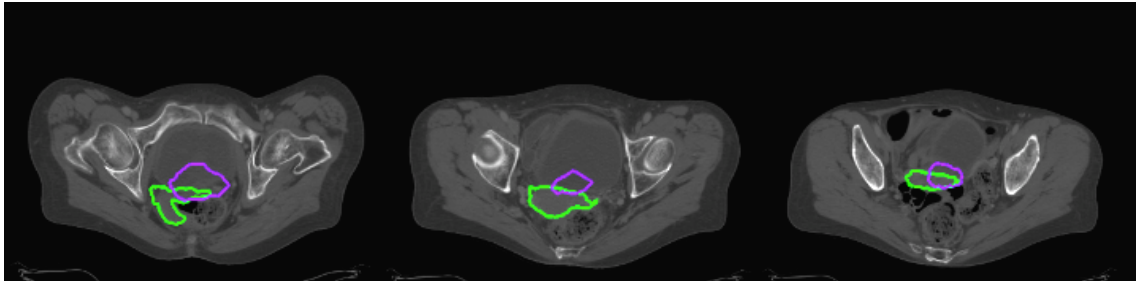


(b) Coronal view (anterior to posterior)

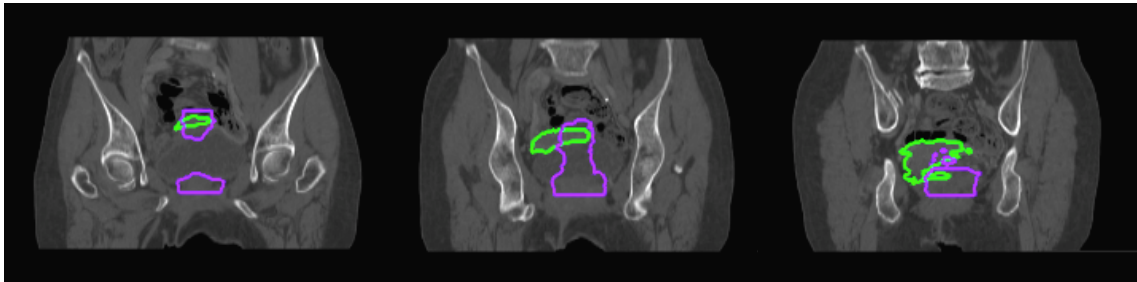


(c) Sagittal view (left to right)

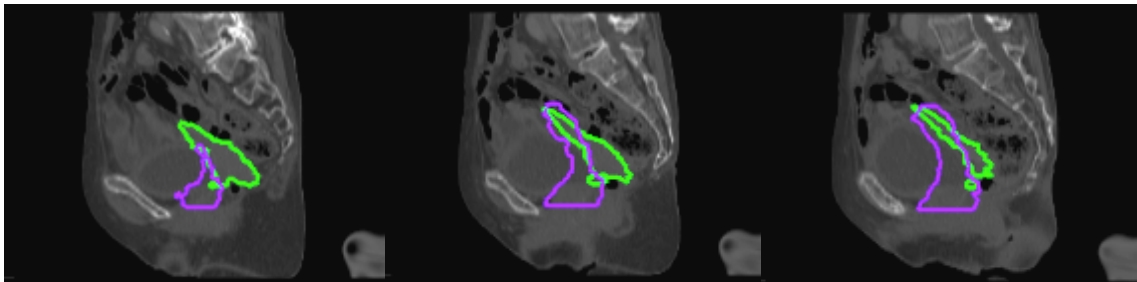
Figure 4.34: Comparison of deformed image and target structure with the good organ overlap.



(a) Axial view (interior to superior)



(b) Coronal view (anterior to posterior)



(c) Sagittal view (left to right)

Figure 4.35: Comparison of deformed image and target structure with the poor organ overlap.

To see performance of the combined registration, especially the effect of addition of biomechanical simulation, intensity-based registration with the exact same transformation model and similarity metrics is also performed to all image sets. Figure 4.36 and 4.37 shows the comparison of both method by hausdorff distance and DSC value, respectively. In both of these graphs, CM refers to the combined method and I refers to intensity-only registration.

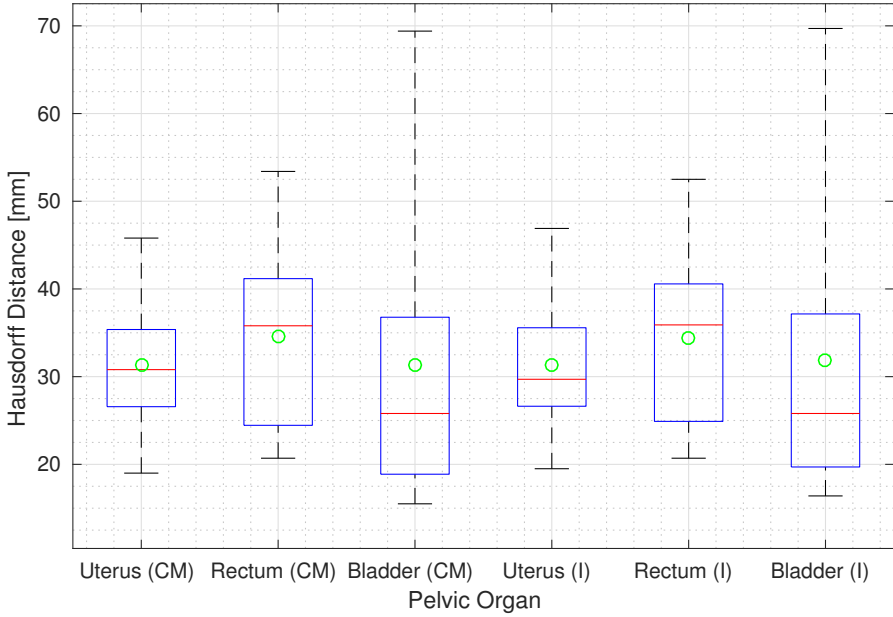


Figure 4.36: Comparison of hausdorff distance from the combined and intensity method

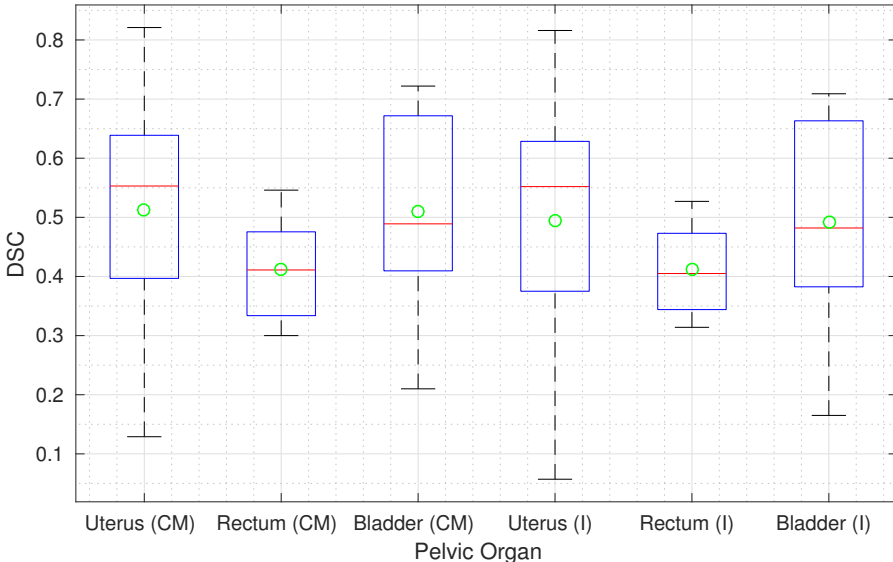


Figure 4.37: Comparison of DSC from the combined and intensity method

From this comparison, it is seen that the overlap of pelvic organ has slight improvement in the combined method. For target organ uterus especially, the average value of DSC as well as the whole range of DSC in registration result is higher than that of the intensity-only method.

The small improvement in organ overlap from registration result is mainly due to the imbalance contribution ratio between biomechanical term and intensity term (which comes from the whole voxels), in which biomechanical term only takes effect around target organ area. However, it shows that by the addition of biomechanical term coming from target organ modeling with tool constraint affects the registration result and can provides a potential correction to the intensity-only registration without manual adjustment.

Further, by observing the amount of uterus overlap improvement in the registration result for all patient cases to the mismatch condition of uterus originally and after biomechanical simulation with FEM, it shows that bigger overlap improvement by the combined method tend to happen to the case with larger uterus mismatch, with the biggest overlap improvement reaches 7.19%. From the sample of P6 and P8 registration explained previously, P6 registration with good DSC value does not show as big improvement as P8 registration with low DSC value when it is compared to the result of original intensity-only registration. In other words, higher DSC value in the combined registration does not mean higher effect of biomechanical term, instead, improvement from the biomechanical term takes effect better for the case with larger organ deformation.

## Chapter 5 Conclusion

This research aims to integrate image information-based registration with biomechanical term to solve image matching with large deformation in organ due to physical intervention, specifically one that occurs in uterus during brachytherapy for cervical cancer treatment. In this thesis, construction of biomechanical simulation and intensity registration-combined method as well as its experiment are performed. Registration process is done based on parametric approach with free-form deformation based on B-spline method as non-rigid transformation model.

Experiments on the proposed biomechanically-combined method starting from volume pre-processing, centerline extraction to determine correspondence between image, biomechanical simulation with finite element method to the final integrated registration are carried out for a set of woman pelvic phantom images and five sets of clinical images from five different patients undergoing EBRT and ICBT. Registration result with phantom image shows an average registration error of  $3.235 \pm 0.804$  mm in left direction,  $3.671 \pm 2.703$  mm in posterior direction,  $5.417 \pm 2.458$  mm in superior direction, and  $7.717 \pm 2.542$  mm in 3D Euclidean. Registration on clinical image results in an averaged similarity value of  $0.513 \pm 0.223$  for target organ uterus,  $0.411 \pm 0.085$  for rectum and  $0.510 \pm 0.032$  for bladder. These values shows slight improvement compared to the original intensity-based registration, which indicates the potential correction from biomechanical term. Further, better improvement of organ overlap by biomechanical term likely happens to the case with larger mismatch of organ.

# Acknowledgement

This work was developed in Oshiro Laboratory, Graduate School of Engineering Science, Osaka University.

I would like to express my deep gratitude to my supervisor, Professor Osamu Oshiro for all the guidance as well as various chance to experience new things given to me. During this period of my graduate school life in Osaka University, particularly as Oshiro Laboratory member, participating in national competition, demonstrating project in international conference, assisting in laboratory events, all are valuable experiences from which I was able to learn many things. I would also like to use this opportunity to express my gratitude to Associate Professor Yoshihiro Kuroda for all the insight, lessons and support given to me in the process of this research, as well as Assistant Professor Shunsuke Yoshimoto and our laboratory secretary Nobuyo Sugiura, who have also been supporting my academic life. I wish to express my gratitude to Assistant Professor Noriyuki Kadoya from Department of Radiation Oncology, Tohoku University Hospital for educating me with medical point of view of this research and providing important information during this study.

My sincere thanks also goes to all Oshiro Laboratory members and seniors, Yuta Ideguchi, Yuki Kato, Daiki Furusawa, Junki Kawaguchi, Takahiro Kato, Shun Hinatsu, Tatsuyuki Kuwatani, Hiroki Kato, Ryohei Hosoda, Hiroshi Takemura, Akifumi Haraguchi, Yuki Mataga, Kaoru Kataoka, Yasuyuki Yamada, Toshiki Hachiya, Yuki Yoshimura, Takuya Sonoda, Takumi Kato, Kazuyuki Fukuda and Naoki Nishida. Spending my daily life with them, while learning and having fun together is a great pleasure for me.

I am also grateful for the funding source that allows me to pursue my graduate school studies, The Ministry of Education, Culture, Sports, Science and Technology (MEXT) Japan. Finally, I would like to thank my family, friends and colleagues for the prayers, moral and technical support throughout this work as well as my life in Japan in general.

The conduct of this work was approved by the ethics committee of Graduate School of Medicine, Tohoku University (No. 2015-1-167).

# Bibliography

- [1] D. Rueckert and P. Aljabar. Nonrigid registration of medical images: Theory, methods, and applications. *IEEE Signal Processing Magazine*, Vol. 27, No. 4, pp. 113–119, 2010.
- [2] J.V. Hajnal, D.L.G. Hill, and D.J. Hawkes. *Medical Image Registration*. CRC Press, 2001.
- [3] T. Okada, R. Shimada, M. Hori, M. Nakamoto, Y. W. Chen, H. Nakamura, and Y. Sato. Automated segmentation of the liver from 3d ct images using probabilistic atlas and multilevel statistical shape model. *Academic Radiology*, Vol. 15, No. 11, pp. 1390–1403, November 2008.
- [4] J. Zhang, J. Wang, X. Wang, and D. Feng. The adaptive fem elastic model for medical image registration. *Physics in Medicine and Biology*, Vol. 59, No. 1, pp. 97–118, 2014.
- [5] C. Kirisits, M.J. Rivard, D. Baltas, F. Ballester, M. De Brabandere, R. van der Laarse, Y. Niatsetski, P. Papagiannis, T.P. Hellebust, J. Perez-Calatayud, K. Tanderup, J.L. Venselaar, and F.A. Siebert. Review of clinical brachytherapy uncertainties: Analysis guideline of gec-estro and the aapm. *Radiotherapy Oncology*, Vol. 110, No. 1, pp. 199–212, January 2014.
- [6] J.M. Ryckman, J.W. Shelton, A.F. Waller, E. Schreibmann, K. Latifi, and R. Diaz. Anatomic structure-based deformable image registration of brachytherapy implants in the treatment of locally advanced cervix cancer. *Brachytherapy*, Vol. 15, No. 5, pp. 584–592, 2016.

- [7] O. Westrand and S. Svensson. The anaconda algorithm for deformable image registration in radiotherapy. *Medical Physics*, Vol. 42, No. 1, pp. 40–53, 2015.
- [8] G. Cazoulat, A. Simon, A. Dumenil, K. Gnep, R. de Crevoisier, O. Acosta, and P. Haigron. Surface-constrained nonrigid registration for dose monitoring in prostate cancer radiotherapy. *IEEE Transactions on Medical Imaging*, Vol. 33, No. 7, pp. 1464–1474, July 2014.
- [9] H. Zhong, T. Peters, and J.V. Siebers. Fem-based evaluation of deformable image registration for radiation therapy. *Physics in Medicine and Biology*, Vol. 52, No. 16, p. 4721, 2007.
- [10] M. Li, E. Castillo, X.-L. Zheng, H.-Y Luo, R. Castillo, Yi. Wu, and T. Guerrero. Modeling lung deformation: A combined deformable image registration method with spatially varying young’s modulus estimates. *Medical Physics*, Vol. 40, No. 8, p. 081902, August 2013.
- [11] T. Zhang, N. P. Orton, T. R. Mackie, , and B. R. Paliwal. Technical note: A novel boundary condition using contact elements for finite element based deformable image registration. *Medical Physics*, Vol. 31, pp. 2412–2415, August 2004.
- [12] P. Li, U. Malsch, and R. Bendl. Combination of intensity-based image registration with 3d simulation in radiation therapy. *Physics in Medicine and Biology*, Vol. 53, No. 17, p. 4621, August 2008.
- [13] H.-P. Lee, M. Foskey, M. Niethammer, P. Krajevski, and M.C. Lin. Simulation-based joint estimation of body deformation and elasticity parameters for medical image analysis. *IEEE Transactions on Medical Imaging*, Vol. 31, No. 11, pp. 2156–2168, November 2012.
- [14] K. K. Brock, M. Hawkins, C. Eccles, J. L. Moseley, D. J. Moseley, D. A. Jaffray, and L. A. Dawson. Improving image-guided target localization through deformable registration. *Acta Oncologia*, Vol. 47, No. 7, pp. 1279–1285, 2008.

- [15] F. F. Berendsen, U. A. van der Heide, T. R. Langerak, A. N. T. J. Kotte, and J. P. W. Pluim. Free-form image registration regularized by a statistical shape model: application to organ segmentation in cervical mr. *Computer Vision and Image Understanding*, Vol. 117, pp. 1119–1127, May 2013.
- [16] M. Staring, U. A. van der Heide, S. Klein, M. A. Viergever, , and J. P. W. Pluim. Registration of cervical mri using multifeature mutual information. *IEEE Transaction on Medical Imaging*, Vol. 28, No. 9, pp. 1412–1421, September 2009.
- [17] F. F. Berendsen, A. N. T. J. Kotte, A. A. C. de Leeuw, I. M. Jùrgenliemk-Schulz, M. A. Viergever, and J. P. W. Pluim. Registration of structurally dissimilar images in mri-based brachytherapy. *Physics in Medicine and Biology*, Vol. 59, pp. 4033–4045, 2014.
- [18] A. Simon, M. Nassef, B. Rigaud, G. Cazoulat, J. Castelli, C. Lafond, O. Acosta, P. Haigron, and R. de Crevoisier. Roles of deformable image registration in adaptive rt: From contour propagation to dose monitoring. In *2015 37th Annual International Conference of the IEEE Engineering in Medicine and Biology Society (EMBC)*, pp. 5215–5218, Aug 2015.
- [19] B. J. Monk, K. S. Tewari, , and W. J. Koh. Multimodality therapy for locally advanced cervical carcinoma: State of the art and future directions. *Journal of Clinical Oncology*, Vol. 25, No. 20, pp. 2952–2965, August 2007.
- [20] H. Zhong, J. Kim, H. Li, T. Nurushev, B. Movsas, and I.J. Chetty. A finite element method to correct deformable image registration errors in low-contrast regions. *Physics in Medicine and Biology*, Vol. 57, No. 11, pp. 3499–3515, 2012.
- [21] J.-P. Thirion. Image matching as a diffusion process: an analogy with maxwell’s demons. *Medical Image Analysis*, Vol. 2, No. 3, pp. 243–260, September 1998.
- [22] J. Canny. A computational approach to edge detection. *IEEE Transactions on Pattern Analysis and Machine Intelligence*, Vol. PAMI-8, No. 6, pp. 679–698, November 1986.

- [23] R. Van Uitert and I. Bitter. Subvoxel precise skeletons of volumetric data based on fast marching methods. *Medical Physics*, Vol. 34, No. 2, pp. 627–38, February 2007.
- [24] R. L. Van Uitert and R. M. Summers. Automatic correction of level set based subvoxel precise centerlines for virtual colonoscopy using the colon outer wall. *IEEE Transactions on Medical Imaging*, Vol. 26, No. 8, pp. 1069–1078, August 2007.
- [25] O.C. Zienkiewicz, R. L. Taylor, and J. Z. Zhu. *The Finite Element Method : It's Basis and Fundamentals*. Elsevier, 2005.
- [26] D. Rueckert, L.I. Sonoda, C. Hayes, D.L.G. Hill, M.O. Leach, and D.J. Hawkes. Nonrigid registration using free-form deformations: application to breast mr images. *IEEE Transactions on Medical Imaging*, Vol. 18, No. 8, pp. 712–721, August 1999.
- [27] S. Lee, G. Wolberg, K.-Y. Chwa, and S.Y. Shin. Image metamorphosis with scattered feature constraints. *IEEE Transactions on Visualization and Computer Graphics*, Vol. 2, No. 4, pp. 337–354, December 1996.
- [28] H. Lester and S.R. Arridge. A survey of hierarchical non-linear medical image registration. *Pattern Recognition*, Vol. 32, No. 1, pp. 129–149, 1999.
- [29] Z. Xie and G.E. Farin. Image registration using hierarchical b-splines. *IEEE Transactions on Visualization and Computer Graphics*, Vol. 10, No. 1, pp. 85–94, January 2004.
- [30] S. Klein, M. Staring, K. Murphy, M.A. Viergever, and J.P.W. Pluim. elastix: A toolbox for intensity-based medical image registration. *IEEE Transactions on Medical Imaging*, Vol. 29, No. 1, pp. 196–205, January 2010.
- [31] G. W. Pearsall and V. L. Roberts. Passive mechanical properties of uterine muscle (myometrium) tested in vitro. *Journal of Biomechanics*, Vol. 11, pp. 167–176, 1978.
- [32] S.M. Duma, D.M. Moorcroft, J.D. Stitzel, and G.G. Duma. Evaluating pregnant occupant restraints: the effect of local uterine compression on the risk of fetal injury. In

*48th Annual Proceedings, Association for the Advancement of Automotive Medicine (AAAM)*, September 2004.

- [33] H. Mahmoud, A. W. Johnson, E. K. Chien, M. J. Poellmann, and B. McFarlin. System-level biomechanical approach for the evaluation of term and preterm pregnancy maintenance. *Journal of Biomechanical Engineering*, Vol. 135, pp. 021008–1 – 021008–11, February 2013.
- [34] W.R. Crum, O. Camara, and D.L.G. Hill. Generalized overlap measures for evaluation and validation in medical image analysis. *IEEE Transactions on Medical Imaging*, Vol. 25, No. 11, pp. 1451–1461, November 2006.
- [35] D. P. Huttenlocker, G. A. Klanderman, and W. J. Rucklidge. Comparing images using the hausdorff distance. *IEEE Transactions on Pattern Analysis and Machine Intelligence*, Vol. 15, No. 9, pp. 850–863, September 1993.

# Achievement

- International Conference

1. Nadhifa Ayunisa, Yoshihiro Kuroda, Noriyuki Kadoya, Shunsuke Yoshimoto, Osamu Oshiro. Deformable Image Registration Method Using Internal Organ Constraint in Cervical Cancer Radiotherapy Case. International Forum on Medical Imaging in Asia (IFMIA) 2017, Okinawa, January 2017.

- Domestic Conference

1. Nadhifa Ayunisa, Yoshihiro Kuroda, Noriyuki Kadoya, Shunsuke Yoshimoto, Osamu Oshiro. A Proposal in Biomechanically-combined Deformable Image Registration for Cervical Cancer Radiotherapy. Research Meeting of Medical and Biological Imaging, Osaka, March 2016.
2. Nadhifa Ayunisa, Yoshihiro Kuroda, Noriyuki Kadoya, Shunsuke Yoshimoto, Osamu Oshiro. Tool-constrained Biomechanically-combined Deformable Image Registration for Cervical Cancer Radiotherapy. The Japanese Society of Medical Imaging Technology (JAMIT) Annual Meeting 2016, Chiba, July 2016.

- Other

1. Nadhifa Ayunisa. Integrated Deformable Image Registration using Cervical Cancer Radiotherapy Tool Constraints. Bioengineering Colloquium, Osaka, July 2016.